The Dissertation Committee for Adam Dudley Lewis Certifies that this is the approved version of the following Dissertation:

APPLICATION OF OPTICAL COHERENCE TOMOGRAPHY FOR IMPROVED IN-SITU FLAW DETECTION IN NYLON 12 SELECTIVE LASER SINTERING

Committee:

Joseph J. Beaman, Co-Supervisor

Thomas F. Edgar, Co-Supervisor

Thomas Milner

Roger T. Bonnecaze

Nathaniel Lynd

APPLICATION OF OPTICAL COHERENCE TOMOGRAPHY FOR IMPROVED IN-SITU FLAW DETECTION IN NYLON 12 SELECTIVE LASER SINTERING

by

Adam Dudley Lewis

Dissertation

Presented to the Faculty of the Graduate School of

The University of Texas at Austin

in Partial Fulfillment

of the Requirements

for the Degree of

Doctor of Philosophy

The University of Texas at Austin

May 2019

Dedicated to my parents and my wife, Farahn.

Acknowledgements

This work could not have been accomplished without the contributions of the many supportive individuals with whom I have had the opportunity and privilege to interact. In particular I credit my parents for instilling in me a desire to earn an advanced degree, for instilling in me a love of learning and information. I appreciate their constant support, love, and encouragement in scholastic activities since birth. The support and encouragement of my wife and loving companion, Farahn, helped motivate me through this process. I also appreciate the love, support, and guidance of my siblings as I earned this degree.

I also acknowledge and thank my many lab mates for their help in completing this work. Tim Phillips was instrumental in helping to fill my gaps in mechanical and design knowledge as needed, and for assisting me by designing and fabricating the 2D OCT stage on the LAMPS machine. Austin McElroy's work with the OCT software, data management, and OCT/position hardware synchronization was invaluable. Michael Gardner, Nitesh Katta, and Arnold Estrada helped educate me on the fundamentals of optical coherence tomography, performed initial work with me, and were generally available for my many optical coherence tomography questions. I appreciate the support, encouragement, and comradery of the other graduate students in my research group including Scott and Patrick Snarr, Debbie Hagan, Doug Sassaman, Trevor Ricker, Sam Taylor, Alex Nettekoven, and Joe Nissen.

I have had the opportunity to work with world class advisors and mentors during my time at UT Austin. I appreciate the expertise from Dr. Joseph Beaman in the area of additive manufacturing, as well as the guidance, support, and freedom to perform research

of interest to me. Additionally, I am greatly indebted to Dr. Scott Fish for his guidance and support in my research. His leadership ability and encouragement inspired me to continue during times when research was not progressing as hoped. Additionally, Dr. Thomas Milner's efforts consulting with me on this research, despite not being a formal advisor, was incredibly helpful.

Abstract

APPLICATION OF OPTICAL COHERENCE TOMOGRAPHY FOR IMPROVED IN-SITU FLAW DETECTION IN NYLON 12 SELECTIVE LASER SINTERING

Adam Dudley Lewis, PhD

The University of Texas at Austin, 2019

Co-Supervisors: Joseph Beaman, Thomas Edgar

Despite significant advances made since the inception of selective laser sintering (SLS), many of the same problems identified by early researchers including high part porosity, inadequate surface finish, and part strength uncertainty persist today. Because of these challenges, quality validation and improved process control continue to be identified as critical areas of improvement in industry roadmaps. To address these issues, an optical coherence tomography (OCT) sensor is investigated for feasibility of use in in-situ flaw detection in SLS. Benchtop OCT imaging of nylon in solid, liquid, and resolidified phases revealed subsurface imaging through liquid and resolidified nylon material was possible.

Subsequent benchtop imaging showed that multiple-scattering was the cause of an imaging artifact which contributed to the limited imaging depth in nylon powder. Additionally, nylon powder was continuously imaged before, during, and after melting and resolidification. The resulting images showed scattering was consistent with the presence of crystalline spherulites, suggesting the spherulites are a strong source of scattering in the nylon 12.

An OCT sensor was subsequently mounted on a production-sized research SLS machine. Design and implementation information is detailed including artifact correction and noise subtraction strategies. The OCT sensor is then used to detect various common defects in the SLS process. Imaging single layer individual scanlines revealed deeper melt depth due to overheating from galvo deceleration near the end of the scan lines. Additionally, surface curl was able to be quantified and visualized for a build. Finally, an SLS build was performed at higher powder bed temperatures. OCT images collected from the build were compared with X-ray computed tomography (CT) images, and many of the pores in the OCT images are shown to agree well with those detected in the CT images. One pore in the dataset was much larger than the others in the part. This caused the author to hypothesize that a different mode was responsible for creating these pores which a subsequent build confirmed. A summary of contributions and future work is also listed.

Table of Contents

List of Tables

List of Figures

Chapter 1: Introduction

1.1 Background

1.1.1 Selective Laser Sintering

Selective Laser Sintering (SLS) is a powder bed fusion additive manufacturing process developed at UT Austin in the late 1980's and early 1990's. It was one the first commercialized additive manufacturing technologies. SLS continues to be relevant as an additive technique in various industries including aviation and the 3D printed medical devices market among others in part due to its ability to produce parts comparable to those created by injection-molding. A schematic demonstrating how the SLS process works is shown in Figure 1 from Gibson et al [1].

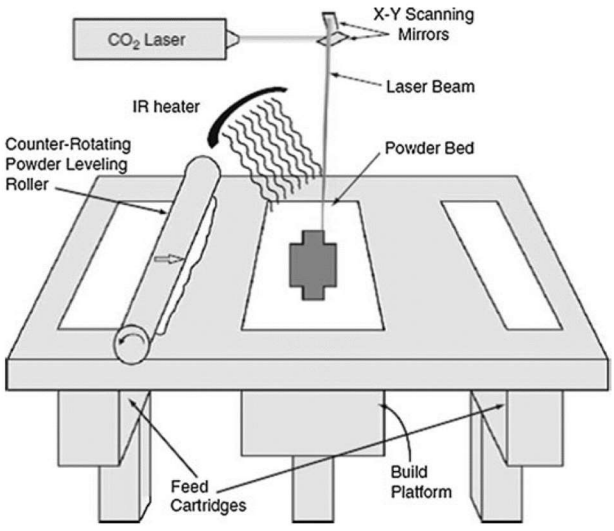

Figure 1: Selective Laser Sintering Schematic [1]

During the build process, the roller will spread a thin (often 200 μm or less) layer of semicrystalline polymer powder on the powder bed. The powder is then heated to within about 10°C of its melting point by an IR heater. Next, a laser beam directed by a set of scanning mirror galvanometers is used sinter a cross-section of the part being built. After sintering, a new layer of powder is spread and heated and the next cross-sectional layer of the part is sintered to itself as well as the layer below. These steps are repeated many times until the part is completely built. Finally, the part is cooled slowly in order to prevent large thermal stresses from accumulating and causing warpage in the part.

The powder materials used in the SLS process are typically semicrystalline with nylon 12 being the most common. As mentioned, the nylon 12 is a powder, melt, and solidified part at various times in the SLS build process. The crystallinity of the nylon varies in each of these phases as well. Various researchers have measured crystallinity values in nylon powder with values ranging from 45-51% [2–6]. The crystals in the lased powder are largely melted during the build phase. Then, the nylon solidifies as it recrystallizes during a cooling period typically on the order of 10 hours. This results in crystallinity of 21-31% in the cooled parts depending on build conditions [2–7].

The recrystallization and solidification of the melted nylon in SLS occurs through the formation of crystalline structures known as spherulites. Spherulites form as crystalline lamella consisting of aligned polymer chains grow spherically outward from nucleation sites and amorphous polymer regions fills the area between lamella as shown in Figure 2 [8]. The degree of crystallinity of SLS parts and the size of such spherulites are affected by the cooling rate. Faster cooling times result in a lower degree of crystallinity and smaller

spherulites while slower cooling times result in a higher degree of crystallinity and larger spherulites [9].

Though a variety of defects may exist in SLS parts, curl and part porosity defects are of particular importance to this work, and are elaborated upon below. There are various mechanisms of curl in the SLS process. This paper will deal only with one, which will be called surface curl. This type of curl is described by Goodridge et al. [3] and is summarized here. In the SLS process, if the powder bed temperature is too low, thermal gradients will cause the edges of the sintered area to curl upwards. This curled region is problematic when manufacturing parts with SLS because if the curl is severe enough, the raised region of the part will catch on and be dragged by the powder spreading element as it travels across the powder bed. This prevents subsequent layers from being sintered in the correct positions relative to the dragged, previously sintered layers.

Porosity within a part decreases the effective cross-section, and in turn decreases the strength of the part. This has been demonstrated by several researchers in SLS parts specifically [10,11]. The ability to detect porosity during a build is an important step towards qualifying the integrity of SLS parts as they are being built as well as researching strategies to reduce or eliminate pores. OCT images are formed as light reflects off of material or phase interfaces in a sample. Pores within a melted nylon region in an SLS part during the build are such an interface, and given a high enough signal, should show up in OCT images.

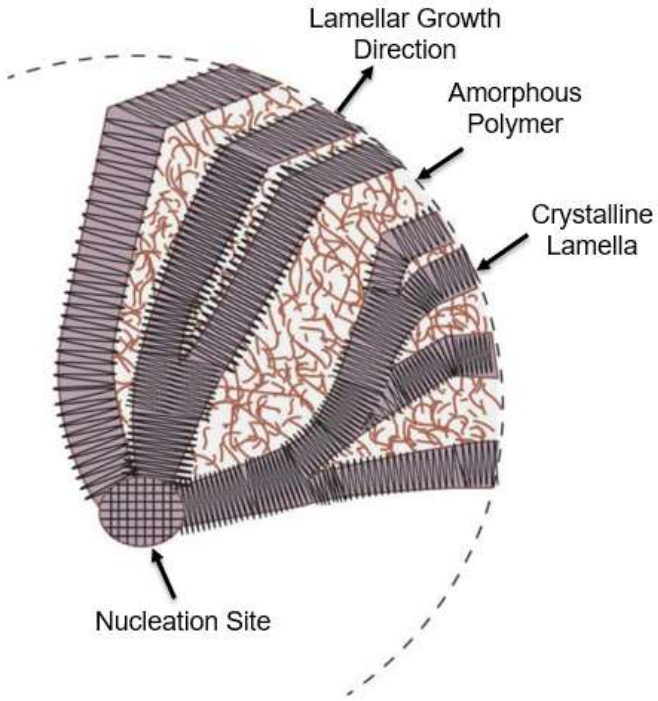

Figure 2: Illustration of a semicrystalline polymer spherulite.

1.1.2 Optical Coherence Tomography

As discussed in Section 1.2, improved process control is vital for the advancement of Selective Laser Sintering. The technology investigated in the present work for improved process sensing in the SLS process is optical coherence tomography (OCT). Optical coherence tomography (OCT) is an established medical imaging technique based on coherence interferometry commonly used in biomedical optics and medicine. In that application, OCT has the ability to provide real time subsurface visualization of human tissues at sub 10μm resolution. OCT data can be used to produce cross-sectional and volumetric images from magnitude and echo time delay data of backscattered radiation as

shown in Figure 3. Figure 4 illustrates some of the terminology commonly used in OCT images including in this paper.

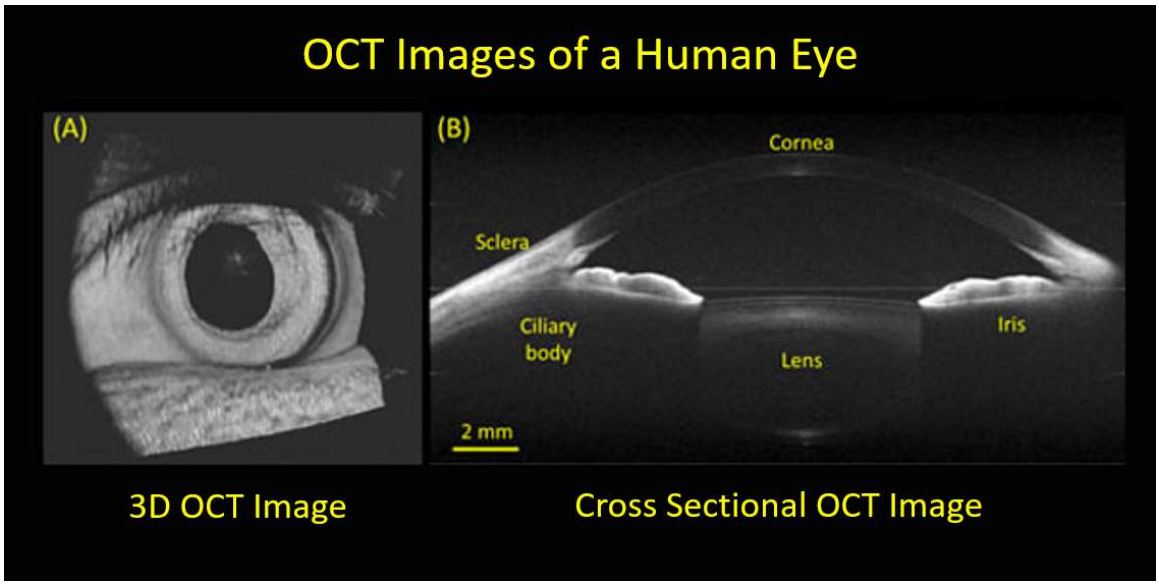

Figure 3: (Left) A volumetric rendering of a human eye (Right) A cross-sectional image of a human eye. Both images were created from data from a typical OCT system [12].

A single OCT scan at a point on the surface of the sample is known as an A-scan and yields depth information at this point. The dotted green line is an example of an A-scan, but each vertical column of data in Figure 4(a) is an A-scan. A collection of subsequent A-scans is called a B-scan and yields a cross-sectional image of the sample. Each panel in Figure 4(a) shows a B-scan. Subsequent B-scans can be combined to yield a 3D representation of the sample. The backscattered intensity information is typically presented in the false color of B-scans and volumetric renderings. OCT data can also be used to generate a transverse or "en face" image. An en face image can be generated by averaging the pixels corresponding to a certain depth range in each A-scan. The en face

image in Figure 4(b) was generated by averaging each column between the yellow dotted lines shown in Figure 4(a) for each of the B-scans. Each A-scan collapsed down to a single pixel and the 3-dimensional dataset consisting of many B-scans collapsed down to a 2D en face image. The data indicated by the yellow dotted line in Figure 4(b) was generated from the B-scan shown at the front of Figure 4(a). The terms A-scan, B-scan, and en face image are used throughout this work as described here.

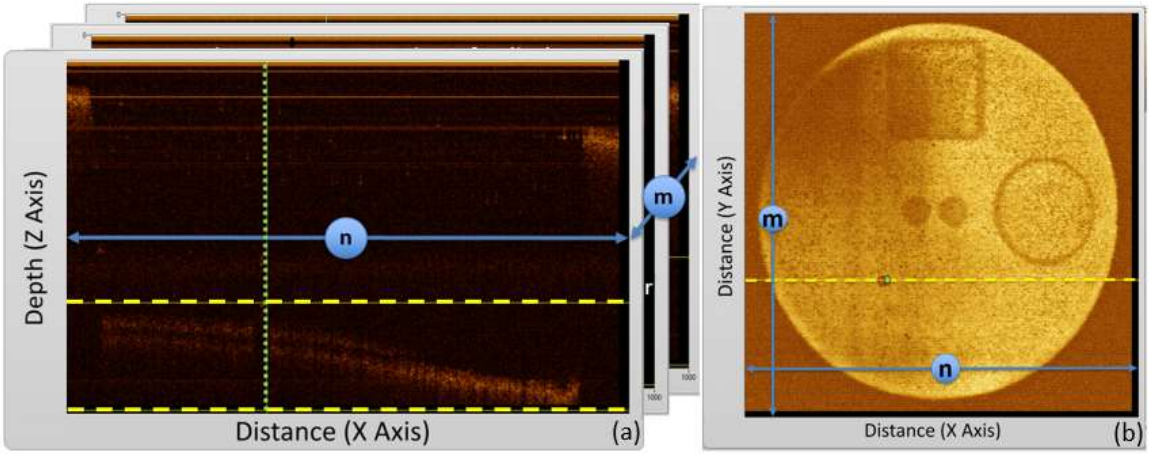

Figure 4: (a) Various B-scans (b) An en face OCT image

Figure 5 illustrates some basic OCT concepts. In OCT, light from a laser is split into "sample" and "reference" beams. The reference beam is split from the source light and serves as a reference time delay for light returning from the sample. The sample beam is forward scattered and possibly absorbed as it propagates into the media of interest. Some radiation entering the sample is backscattered and re-combines with the reference beam forming an interference between these beams that is measured by a photodetector. From this measurement, spatial information about the sample can be obtained. Interfaces where

the index of refraction changes suddenly (large longitudinal gradient), including variations in material phase and material type are often detectable with OCT.

There are several different types of OCT systems. An optical fiber-based swept source OCT system (SS-OCT) was used for the experiments in this section. Detailed information about other types of OCT can be found in [13]. Additional SS-OCT specific background information is provided below.

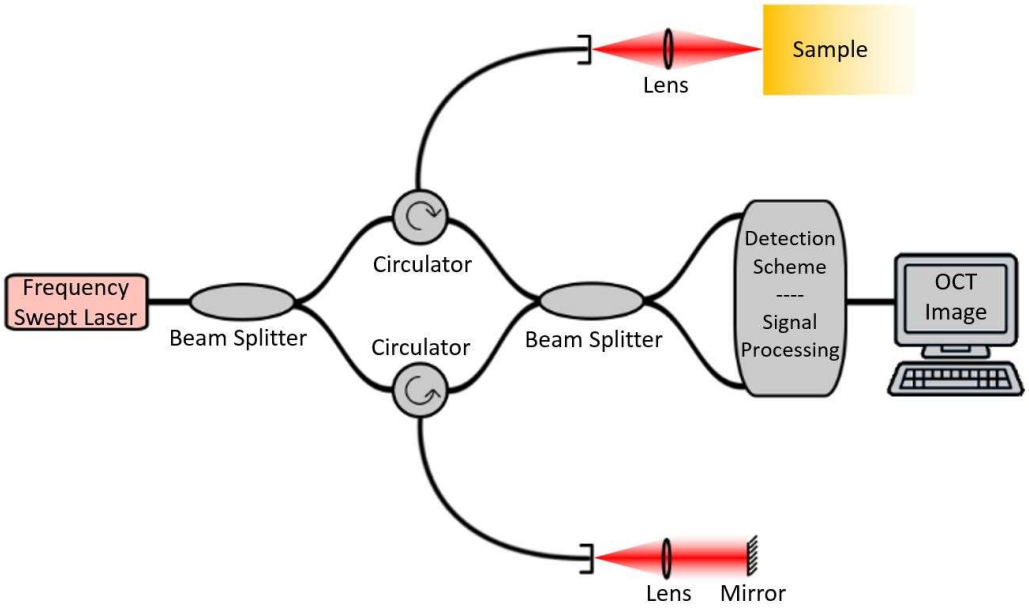

Figure 5: A schematic of a simple two-beam swept source OCT system (SS-OCT)

In SS-OCT systems, the wavelength of the radiation emitted by the laser changes in time as it sweeps across a frequency range during each A-scan. The light in the sample arm is configured to travel slightly longer than that in the reference arm. The difference in path length between light in reference and sample paths causes the phase of the interference fringes to vary as the optical source frequency, ν, varies. The phase, ϕ, of the interference

between reference and sample paths varies as $\phi = 2\pi c \tau \nu$ where c is the speed of light, ν is the optical frequency and τ is the time delay between sample and reference paths. Because light in the sample beam travels variable path length delays, τ, depending on how far into the sample it penetrates before back reflecting, a Fourier transformation is necessary to allow the individual path length delays in the interference signal to be separated out yielding the axial scan information (echo magnitude vs. time delay).

1.1.3 LAMPS Machine

Research into improved sensing, monitoring, and control of the SLS process is difficult with most commercial SLS machines due to limited sensing abilities, the inability to install custom sensing equipment, and the inability to implement custom control strategies using the printer's commercial operating software. The SLS machine used in this research is the Laser Additive Manufacturing Pilot System (LAMPS) machine. The LAMPS machine was designed and built at The University of Texas at Austin as an open architecture SLS printer to allow increased monitoring and control of the SLS process variables. Typically, feedback data in commercial SLS machines are limited to a few pyrometers and thermocouples. However, the LAMPS machine is outfitted with over 40 strip heaters with associated thermocouples, both visual and infrared cameras, and permits the addition of non-standard data acquisition elements (such as OCT) as well as custom control strategies as needed. A more complete description of the LAMPS System can be found in Wroe et al. [14] and Fish et al. [15]. Figure 6 shows the LAMPS machine as well as a cross-section of the build chamber.

1.2 MOTIVATION & PURPOSE

Despite significant advances made since the inception of SLS, many of the same problems identified by early researchers including high part porosity, inadequate surface finish, and part strength uncertainty persist today [16] due to the complex phenomena involved in the SLS process. Much of the difficulty in correcting these shortcomings stems from the relative lack of sensors and feedback control compared to traditional manufacturing techniques. Because of these challenges, quality validation and improved process control continue to be identified as critical areas of improvement in industry roadmaps [17,18].

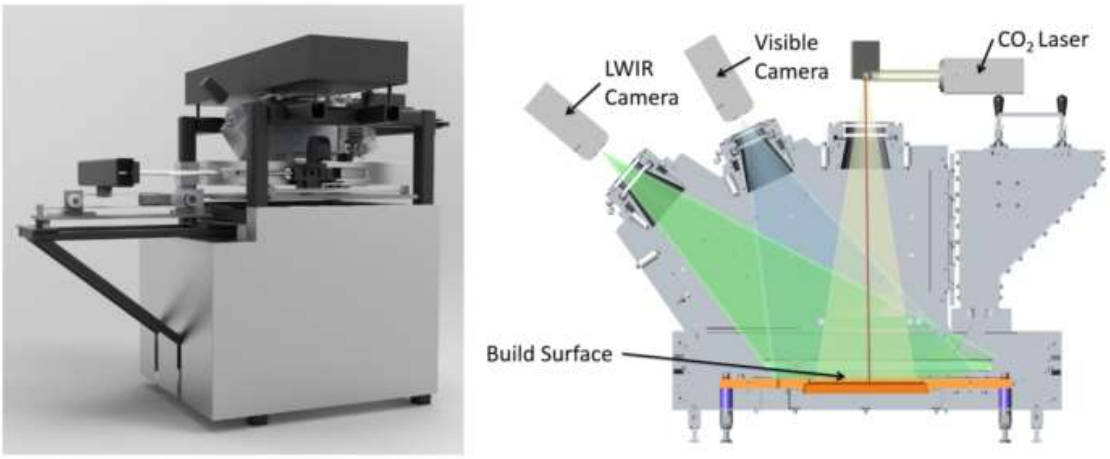

Figure 6: (Left) External View of LAMPS CAD geometry [14] (Right) LAMPS Build Chamber Cross-section

This recognition has resulted in the application of a wide variety of additional process sensors on research machines used for SLS and the related process, Selective Laser Melting (SLM). Most of the machine improvements center around the use of high speed visual and infrared cameras, photodiodes and additional infrared pyrometers (add

references?). However, these measurement methods are not able to provide depth information without additional a priori knowledge of the system. Recently, direct measurement of relevant depth information such as melt pool depth has begun to be explored with imaging techniques based on laser interferometry [19–23] such as optical coherence tomography (OCT).

Research using OCT and the related low coherence imaging technique Inline Coherent Imaging (ICI) in Laser Powder Bed Fusion (LPBF) AM processes is fairly limited. In 2014, Neef et al. [19] used ICI to measure the powder bed and melt track topologies in SLM. Powder and SLM melt track were differentiated with ICI and potential uses of ICI in SLM were speculated. The following year, Kanko et al. [20] used ICI to investigate melt pool morphology. Although, vapor channels present during the melting process permitted the measurement of keyhole depth at higher melting laser powers, ICI was not able to image through the melt pool or metal powder due to high absorption by metals of the imaging wavelengths used. In 2015, Guan et al. [21] showed subsurface OCT imaging of nylon 12 SLS parts was possible by imaging intentionally placed hollow regions 200-400μm below the part surface. Guan et al. also suggested the use of OCT imaging as a possibility for real-time, in-situ process monitoring and control in SLS. In 2016, Guan et al. [22] demonstrated the ability to detect near subsurface unsintered and undersintered powder regions in SLS nylon 12 parts.

Although several of these researchers used OCT for surface imaging of metals, they were not able to image beneath the surface due to the high reflectivity of metals. In the ex-situ experiments, Guan did show that subsurface imaging of at least 200-400 microns depth

is possible in Nylon 12 [22]. Given that SLS is a layer-wise process with layer thicknesses around 100 microns, the prospect of imaging the volumetric entirety of parts is promising with an in-situ OCT system. Such a subsurface imaging system used in SLS may permit detection of many of the flaws common to SLS parts including inaccurate dimensional accuracy, part porosity, as well as the surface curl defect. With that stated, the present work has several main objectives:

1 Establish feasibility of the use of OCT as an in-situ sensor capable of imaging the volumetric entirety of nylon 12 SLS parts

2 Integrate an OCT system with an SLS machine for experimental data collection

3 Use the integrated OCT/SLS machine to detect defects common to SLS.

1.3 OVERVIEW

The work presents several studies performed to accomplish the stated objectives above. Much of the information in Chapters 2-7 has been published in referenced journals and conference proceedings with each chapter containing its own introduction and conclusions. The chapters are summarized as follows:

Chapter 2: Establishing Feasibility of Optical Coherence Tomography as an In-Situ Sensor in Selective Laser Sintering of Nylon 12

Before spending the time, effort, and money to fit a OCT sensor onto an SLS machine, feasibility of OCT as a potential in-situ sensor in the SLS process was verified

with benchtop experiments. To accomplish this, Nylon 12 was imaged with OCT in the relevant phases in which it is found in the SLS process, namely as powder prior to any processing, as a liquid, and as a resolidified part.

Chapter 3: Understanding and improving optical coherence tomography imaging depth in selective laser sintering nylon 12 parts and powder

Chapter 3 expands the understanding of the optical properties of the SLS Nylon 12 material as well measuring and improving the imaging depth of nylon 12 powder, and sintered material with an index matching liquid. A small amount of powder is lased in a cuvette and imaged throughout the melting and resolidification process and the crystalline spherulites are identified as a strong cause of scattering in SLS Nylon 12 parts.

Chapter 4: Integrating Optical Coherence Tomography on the LAMPS Machine

Chapter 4 documents the integration of the OCT System with an SLS machine. The optical design is discussed as well as the hardware configuration and post processing algorithms necessary for rapid, automated post processing of the data for improved utility and visualization of the OCT data.

Chapter 5: In-situ OCT Measurement of Single Scan Lines

Chapter 5 uses the integrated OCT/SLS machine setup detailed in Chapter 4. The in-situ OCT sensor is used on the SLS machine to image single scan lines at various

powers. Individual scan lines are the building blocks of every build, and uneven scan line heating is evident in the collected OCT images.

Chapter 6: In-situ Curl Detection using Optical Coherence Tomography

In Chapter 6, an experiment is performed which induces surface curl in several Nylon 12 parts during an SLS build. The integrated OCT/SLS setup is used to collect images of and quantify the amount of curl in the build at each location in the build.

Chapter 7: In-situ Porosity Detection with Optical Coherence Tomography

In Chapter 7, the integrated OCT/SLS setup is used to collect images of a Nylon 12 SLS part during fabrication. After production, the part is scanned with X-Ray Computed Tomography (CT). There is agreement between some of the pore locations detected in the OCT and XCT data.

Chapter 8: Conclusions and Future Work

Chapter 8 contains a summary of the conclusions of this work and discusses suggestions of future next steps to expand on the presented work.

Chapter 2: Establishing Feasibility of Optical Coherence Tomography as an In-Situ Sensor in Selective Laser Sintering of Nylon 12

2.1 Introduction

The purchase and integration of an OCT System is a significant task in terms of time, effort, and monetary cost. Before expending those resources, it was deemed prudent to establish feasibility of the concept of using OCT in SLS as much as possible with less costly benchtop experiments before proceeding with the OCT/SLS machine integration. If the benchtop experiments proved unfruitful, many resources could have been conserved. As detailed in this chapter, the benchtop study did exhibit sufficient promise for continued work. During an SLS build of a nylon 12, the nylon exists as a powder, as a liquid, and as a recrystallized part upon cooling. Therefore, in this study, nylon 12 is imaged in each of these states with OCT. The images are analyzed with a special emphasis on imaging depth of the nylon in each state. This chapter is revised and expanded from work published in conference proceedings [23].[1]

[1] This chapter contains work previously published in A. Lewis, M. Gardner, A. McElroy, T. Milner, S. Fish, J. Beaman, In-Situ Process Monitoring and Ex-Situ Part Quality Assessment of Selective Laser Sintering Using Optical Coherence Tomography, in: Process Development, Austin, TX, 2016. In that work, the primary experimental design, imaging, and analysis presented was performed by A. Lewis. The boresighted design for the OCT system was primarily developed by M. Gardner. M. Gardner and A. McElroy provided imaging expertise in taking and analyzing images. T. Milner, S. Fish, and J. Beaman reviewed conclusions, and provided recommendations in a supervisory capacity.

2.2 MATERIALS & METHODS

2.2.1 Powder and Part samples

Several different samples of virgin powder and SLS parts were imaged in a laboratory setting in this work. The powders imaged included 2 commercially available semicrystalline, thermoplastic powders and 1 thermoset oligomer research powder. One of the commercially available powders was nylon 12 with the tradename PA650 from Advanced Laser Materials (ALM). The data sheet provided by ALM gives a particle size range, D10-D90, of 30 to 100 μm and a mean particle diameter of 55 μm. The other commercially available powder was PEEK under the trade name EOS PEEK HP3 from EOS. The data sheet provided indicates an average particle diameter of 60 μm. The thermoset provided to us by the Air Force Research Lab (AFRL) is known as RTM370 Oligomer. The thermoset material has a glass transition temperature of about 140°C and that the crosslink reaction starts at 290°C. No information was provided about the particle size distribution of the thermoset powder. All of the SLS parts imaged were also made from the same virgin, unfilled nylon and PEEK powders in the LAMPS machine.

2.2.2 OCT System

Although only a single OCT system was used for the results presented in this chapter, several others were used for experiments throughout this work. The OCT System in this chapter is named OCT System A to differentiate it with other OCT Systems used in

this later chapters of this work. The design scheme for each of the OCT systems used in this work is given in Figure 7.

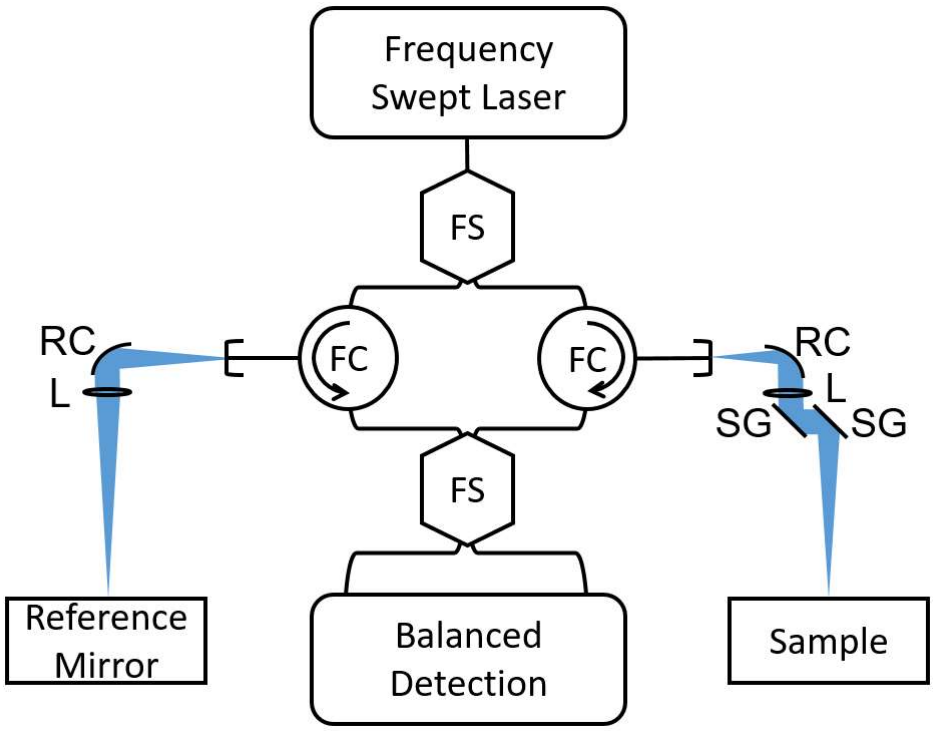

Figure 7: A schematic of the design of the OCT systems used in this work. The systems incorporated a fiber based Mach-Zender interferometer. The frequency swept laser was split into reference (left) and sample (right) arms in a fiber coupler (FS). In each arm of the interferometer, a fiber circulator (FC) directs the beam to a reflective collimator (RC) and a lens (L) focusing the light onto either the sample or the reference mirror. A set of scanning galvanometer mirrors (SG) scans the sample beam over the sample. The reflected light in each arm is collected and directed through the fiber circulator (FC) to another fiber coupler (FS) where the light is detected in a balanced detection scheme.

The OCT system used in these experiments comprised of a commercially available AXSUN swept source laser with details given in Table 1. The lateral resolution is given by the spot size, which was simulated to be 6μm using the optical simulation software,

OpticStudio. The axial pixel resolution was determined by moving the mirror in the sample arm. Using a precision micrometer (Z825B Thorlabs Inc.), the mirror interface was moved 1 millimeter to determine the change in the pixel value. This gave a per pixel movement of 3.75 μm/pixel. The lateral pixel resolution was determined by imaging a ruler and dividing 4mm by the number of pixels between the tick marks and was found to be 16 μm/pixel.

The axial (depth) resolution of OCT System A is defined as the smallest distance that can be discriminated at a refractive index discontinuity. To evaluate the axial (depth) resolution of the OCT system, the mirror's Full Width Half Maximum (FWHM) at the interface between air and the mirror was utilized. The FWHM in pixels was about 1-2 pixels, hence the axial resolution of the system was determined to be about 5.6 ± 2μm.

Table 1: Key Parameters for OCT System A

Swept Source Laser Parameters			
Average Output Power	30 mW	Sweep Rate	100 kHz
Central Wavelength	1310 nm	Wavelength Tuning Range	125 nm
Resolution Parameters			
Axial Spatial Resolution	5.6±2 μm	Lateral Spatial Resolution	6 μm
Axial Pixel Resolution	3.75 μm/pixel	Lateral Pixel Resolution	16μm/pixel

2.3 RESULTS/DISCUSSION

The following selectively laser sintered parts were imaged in a laboratory setting as part of the preliminary ex-situ OCT analysis:

- Various types of virgin powders
- Melted nylon powder in a glass dish on a hot plate
- A nylon 12 tensile bar specimen with a ledge
- half of a nylon tensile bar specimen in which layering was visible
- A PEEK part with noticeable surface pitting.

2.3.1 Virgin Powders

Several similar plastic trays were used for imaging powder. One of the empty plastic trays was imaged first and the thickness of the tray was determined. The tray was then filled with various powders. It was attempted to fill the trays in such a way as to provide a gradual slope in the height of the powder to provide a varying powder thickness. Then the powder was imaged where the powder thickness was smallest. As can be seen in Figure 8, the top and bottom surfaces of the dish were no longer visible through even a small amount of powder.

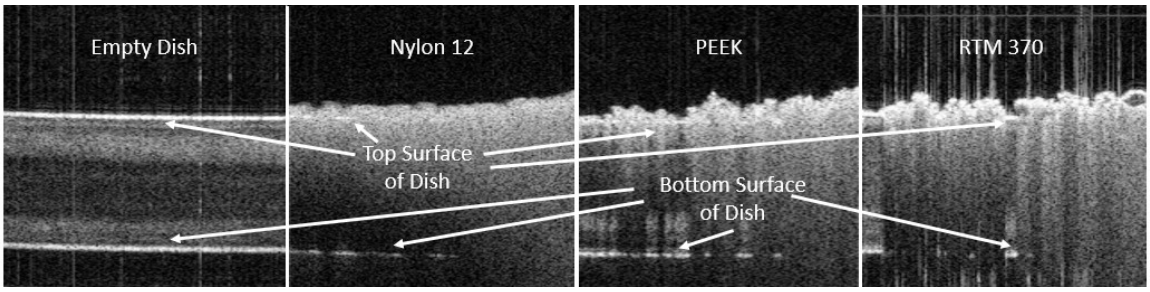

Figure 8 Various powders were imaged. The highly scattering nature of the powders prevented imaging through even a small layer of powder.

The penetration depth of the powders is difficult to ascertain from such data. However, further analysis was performed on the nylon powder below in order to determine the imaging depth of nylon powder in air. As shown at the top of Fig. 3, the top and bottom surfaces of the empty dish were clearly visible. A similar, but separate dish was then filled with nylon powder in such a way as to achieve a powder layer of varying thickness in the dish. The powder was then imaged in an area with the least powder thickness. As can be seen in Figure 9, the top and bottom surfaces of the dish were visible only through a very thin layer of powder as noted previously.

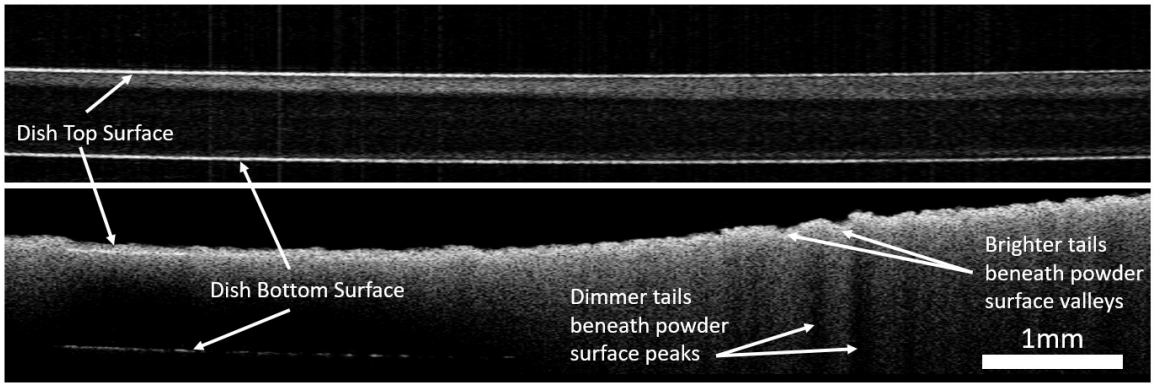

Figure 9: (Top) OCT image of empty dish with top and bottom surfaces labeled. (Bottom) OCT Image of nylon in a similar dish with a signal-tail imaging artifact labeled.

Additionally, a bright "signal-tail" region is visible beneath the powder that was not present in the image of the empty dish. Because these signal tails only occurred where the powder was present suggested that they were caused by multiple-scattering of the OCT laser in the powder particles. The multiple-scattering events would increase the path length of the light before it is collected. Because scattering depth in OCT is determined by the

path length of the light, the multiple-scattering events result in a scattering signal beneath the depth where the reflections occurred. A similar effect had been reported by Veilleux et al. when OCT imaging small glass powder particles and was attributed to multiple scattering as well [24]. It was also observed that signal tails beneath powder surface "valleys" were brighter than tails beneath powder "peaks" as indicated in Figure 10. This is also consistent with multiple scattering as a greater solid angle around a powder surface valley intersects with other nearby powder particles than those around a powder surface peak as illustrated in Figure 10. A greater powder intersecting solid angle means a greater likelihood of a future nearby scattering event that can subsequently couple back in with the OCT system and contribute to the overall brightness of the signal tail in the OCT images.

Typically, the imaging depth could be determined by noting the depth at which the signal is 6 dB above the background signal. The presence of the signal-tail artifact renders this method ineffective. Thus the depth through which the bottom surface of the dish was visible was used as a measure of imaging depth instead. A histogram of the powder thicknesses through which imaging was determined possible is given in Figure 11. The index of refraction of the nylon powder was assumed to be 1.5 based on values reported for other polyamides [24]. Regardless, a liberal imaging distance was obtained by assuming a unity index of refraction. Though the exact histogram obtained was dependent on the choice of threshold intensity values used during the analysis, this analysis gives an indication of the limited OCT imaging depth of nylon powder. Even when assuming a unity index of refraction, the mean penetration depth (48.4μm) was less than the mean powder particle diameter (55μm).

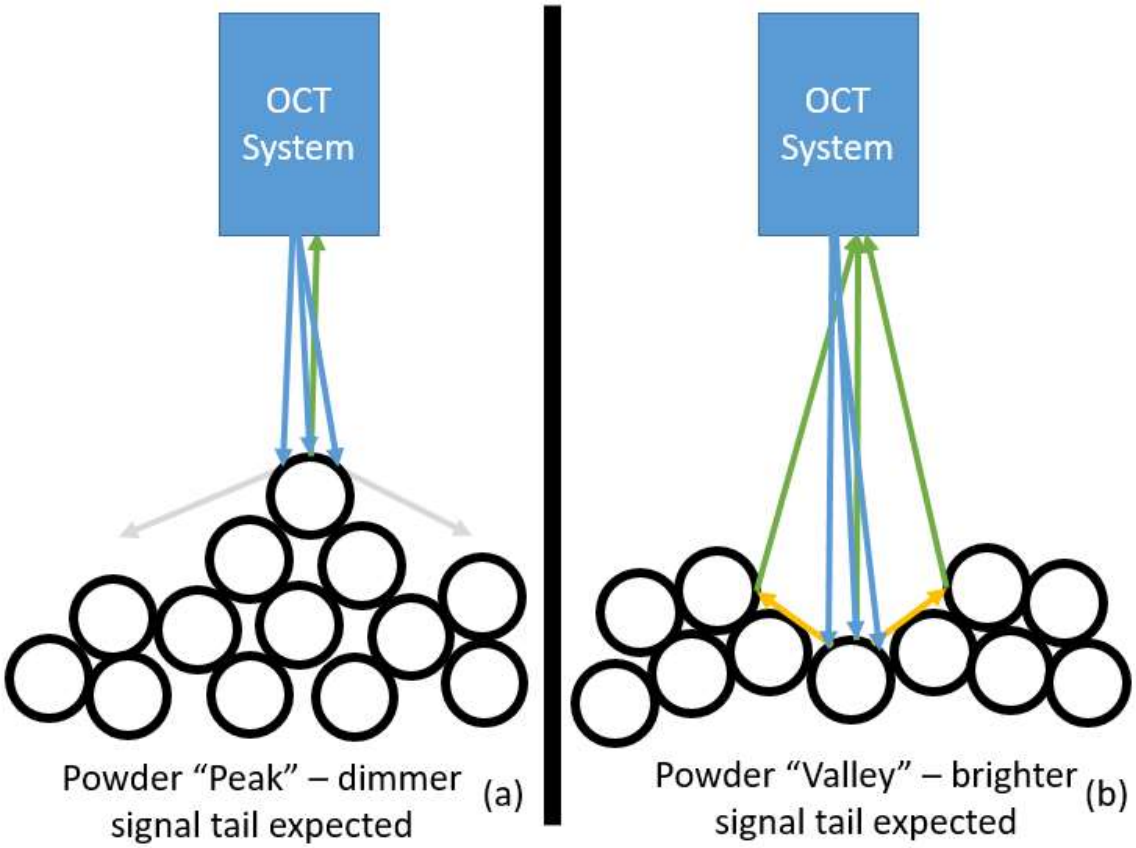

Figure 10 Two OCT systems imaging (a) a powder peak and (b) a powder valley. The blue arrows represent the OCT beam incident on the powder sample. The gray arrows indicate scattered rays which are unlikely to couple back in with the OCT system. The yellow arrows represent multiple scattering rays which eventually couple back in with the OCT system. Green rays represent multiple scattering rays as they are coupling in with the OCT system and thus contribute to the "signal tail" seen in the OCT images.

2.3.2 Liquid Nylon 12

Liquid nylon 12 was also imaged with OCT. To do so, nylon powder was placed in a glass dish and placed on a hot plate set to a temperature above the melting temperature of the powder. The nylon was then imaged continuously until the powder melting was

observed. Figure 12 shows representative images from that data. The same section of powder is being imaged in both Figure 12a and Figure 12b, but Figure 12b was imaged approximately 1 second after Figure 12a.

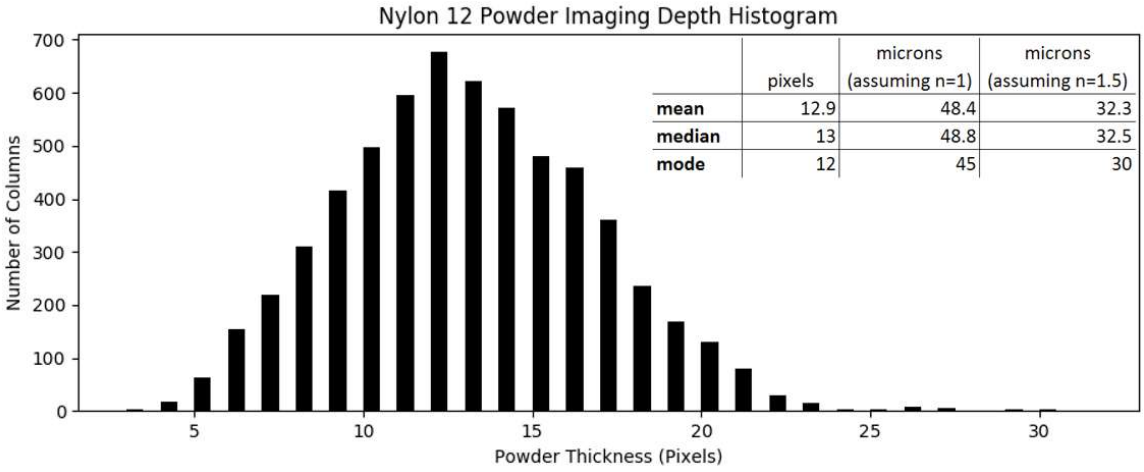

Figure 11 A Histogram showing the powder thickness through which OCT imaging was possible assuming various indices of refraction for nylon 12 powder. The bottom dish was only visible through less than the mean diameter of a powder particle.

2.3.3 Nylon 12 Tensile Bar with Ledge

The nylon 12 part shown in Figure 13 was imaged. The ledge on the part was created inadvertently as the SLS powder roller moved the previously sintered layers slightly while spreading subsequent powder layers. Figure 14 shows the B-scan cross-section of the tip of the ledge.

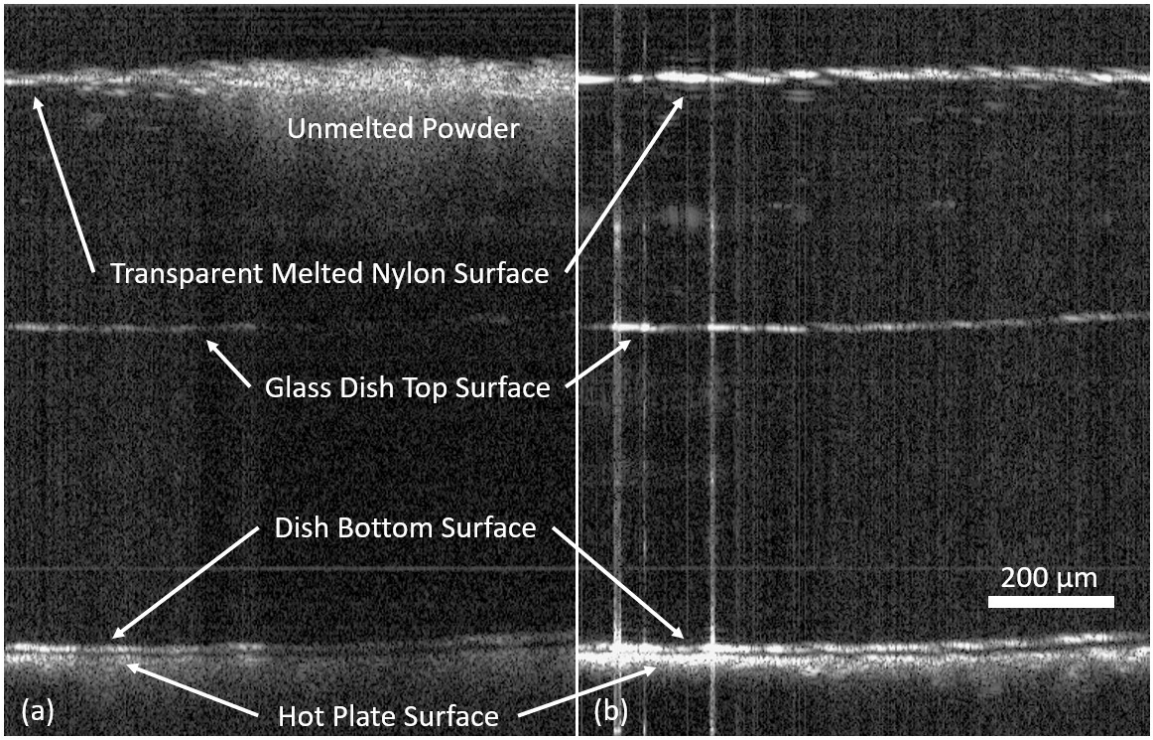

Figure 12: Nylon powder in a dish on a hot plate is shown (a) before all powder has melted and (b) 1 second later after all powder has melted.

The bottom boundary of the ledge is visible in Figure 14. With the refractive index of the sintered part it is possible to calculate the thickness of the ledge. In absence of a measured value for the refractive index of nylon 12, a value of 1.53 was assumed based on the indices of refraction of other types of nylon [25]. Using the assumed index of refraction the ledge thickness at the dotted line was found to be approximately 0.18 mm or nearly 2 layers thick. Even greater imaging depths may have been possible, and imaging depth in nylon SLS parts is studied in further detail in the next chapter.

Figure 13: (Left) View of tensile bar from above (Right) The ledge is apparent on the left of the image when looking at the tensile bar from the end.

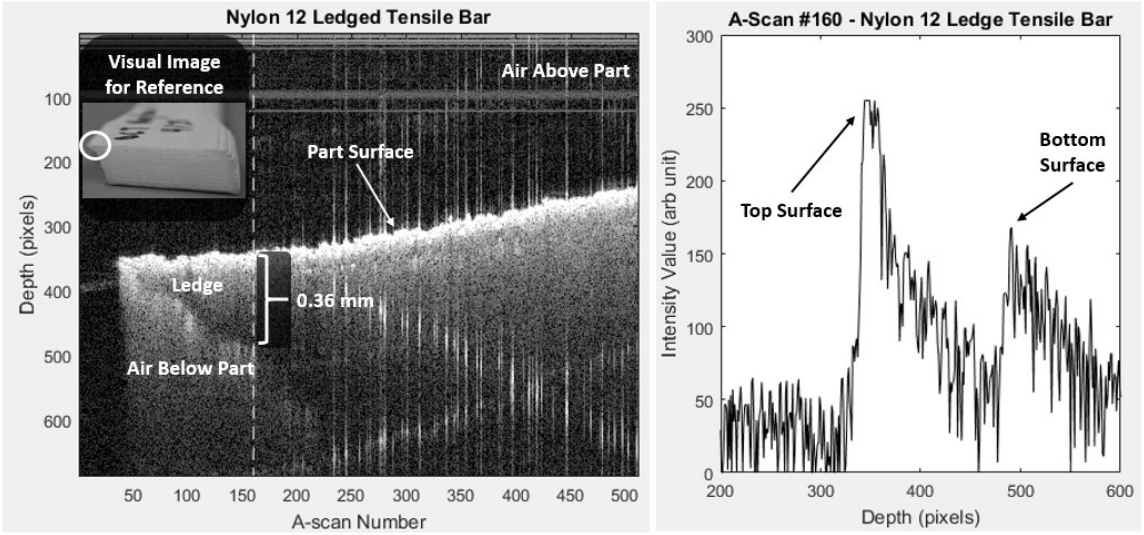

Figure 14 (Left) A single B-scan of the tensile bar ledge is shown (Right) A scaled intensity value from a single A-scan is shown with the top and bottom surfaces of the ledge labeled.

2.3.4 Half of Nylon 12 Tensile Bar

A half nylon 12 tensile bar specimen was also imaged. The tensile bar was built in the xz orientation, and the build was aborted approximately halfway through and no

powder was spread while the tensile bar cooled. This resulted in a flat and noticeably smoother top surface where no unmelted powder particles sintered to this surface. A volume of the smooth top surface was imaged consisting of 512 B-scans each consisting of 512 A-scans. The data was cropped to exclude the edge of the part, the maximum surface pixel of 204,800 A-scans were aligned and then averaged from 10 pixels before the surface peak to 339 pixels afterwards. An image of the part, a sample B-scan, and the average A-scan is shown in Figure 15. Horizontal lines are apparent beneath the surface of the part in the sample B-scan. The average A-scan plot confirms the existence of subsurface horizontal lines of increased intensity. The regularity of the horizontal lines may indicate that they correspond in some way to the build layers of the part though no lines were apparent in the other nylon part imaged.

2.3.5 PEEK Pitted Part

A PEEK part with noticeable pitting on the surface was imaged next. As expected, the surface defects were clearly visible in the OCT images. Defects down to the size of the lateral resolution (commonly < 10μm) of the OCT system should be detectable. Although not performed in the present work, OCT can be used to perform high resolution surface roughness characterization on finished parts. Visual and OCT images are shown below in Figure 16. A cross-section of one of the surface pits is visible in the OCT image.

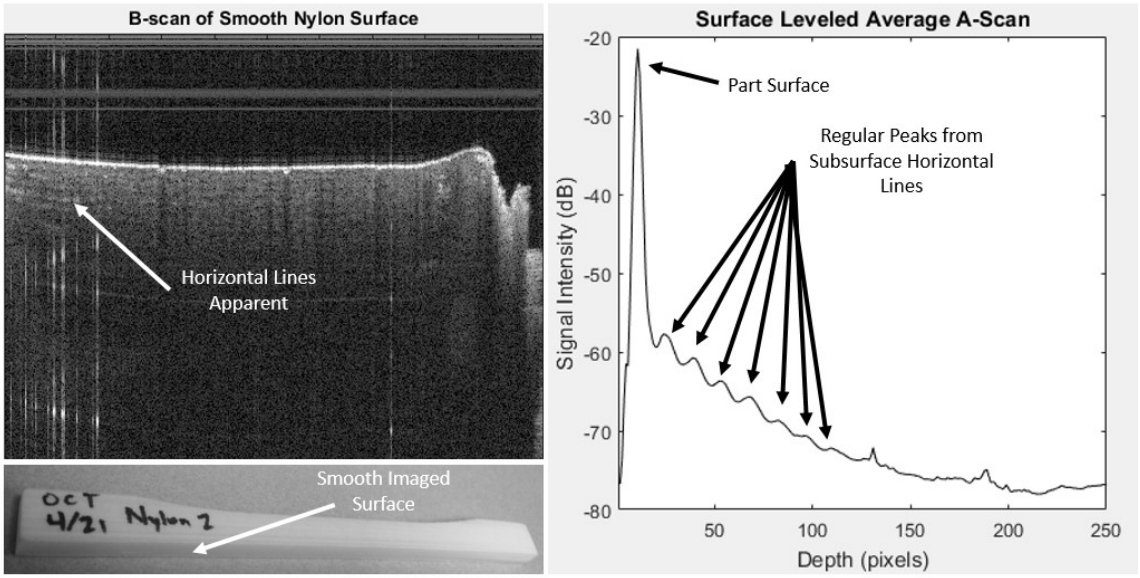

Figure 15 (Top Left) A B-scan of the smooth nylon 12 surface (Bottom Left) Visual of the imaged part (Right) Surface Leveled Average A-scan

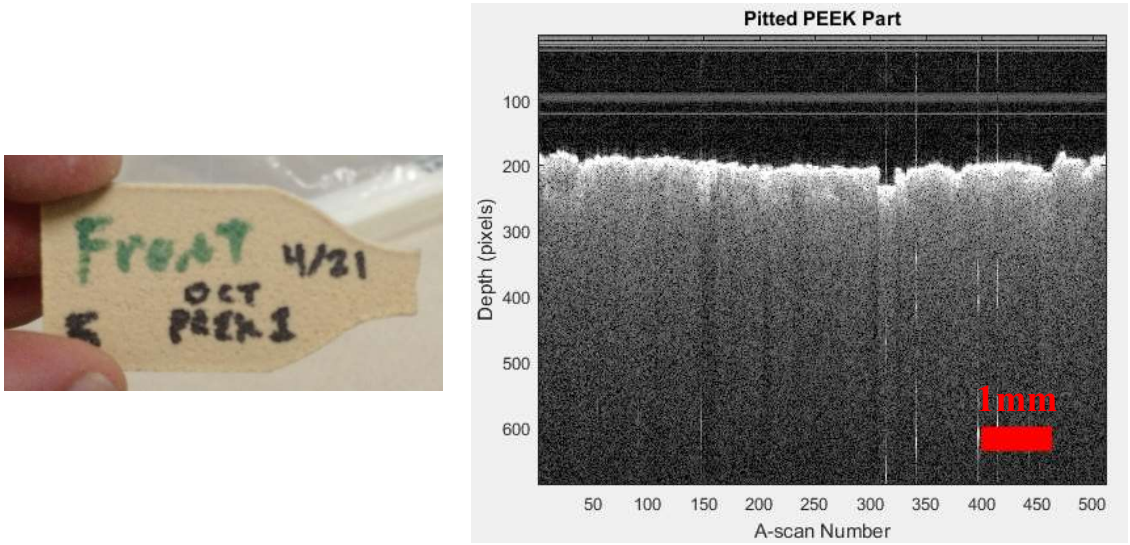

Figure 16 (Left) A pitted PEEK part (Right) OCT image of a pit in the surface of the par

2.6 CONCLUSIONS

Various virgin powders, liquid nylon, and sintered parts were imaged with OCT in a laboratory setting. The various powders were all shown to be highly attenuating. An artifact appeared beneath the powder that was caused by multiple scattering. Additional analysis was performed on the nylon virgin powder showing that attenuation limits the OCT penetration depth to less than 50 microns. Melted nylon 12 appeared transparent in OCT images, and a depth of greater than 400 microns was imaged with OCT. Three sintered SLS parts were also imaged. It was possible to image through about 0.18 mm of the first sintered nylon SLS part. Imaging the second SLS part showed scattering regions below the surface of the part corresponding to the layers in the SLS build process. Finally, a PEEK part which exhibited surface pitting was imaged. The surface roughness was able to be detected in the captured OCT images.

Chapter 3: Understanding and improving optical coherence tomography imaging depth in selective laser sintering nylon 12 parts and powder

3.1 Introduction

It is the objective of this paper to provide a more thorough understanding of the fundamental optical phenomena necessary in order to understand both the capabilities and limitations an OCT sensor has when used in conjunction with selective laser sintering. A signal tail defect was observed from the study in Chapter 2 and liquid nylon was much more transparent to OCT wavelengths than the sintered material or the virgin powder nylon. The cause of the signal tail defect was hypothesized to be multiple scattering and some evidence was given to support that hypothesis, but it was still unclear whether the multiple scattering resulted exclusively from interparticle scattering or whether intraparticle scattering, scattering within a single powder particle, also contributed to the signal tail defect.[2]

In this paper, the cause of the signal tail was identified through imaging of individual powder particles on a mirror as well as bulk powder in an index-matched liquid

[2] This chapter contains work previously published in A.D. Lewis, N. Katta, A.B. McElroy, T.E. Milner, S. Fish, J.J. Beaman, Understanding and improving optical coherence tomography imaging depth in selective laser sintering nylon 12 parts and powder, OE, OPEGAR. 57 (2018) 041414. doi:10.1117/1.OE.57.4.041414 and A. Lewis, N. Katta, A. McElroy, T. Milner, S. Fish, J. Beaman, Investigation of Optical Coherence Tomography Imaging in Nylon 12 Powder, in: Process Development, Austin, TX, 2017. In those works, A. Lewis performed the primary experimental design, imaging, and analysis presented.

and subsequent analysis. A sintered nylon 12 part was then imaged in air and an index-matched liquid, and the imaging contrast was improved when imaged in the index-matched media. Finally, nylon powder was continuously imaged before, during, and after melting and resolidification. A laser was used to melt the bulk powder in order to increase the fidelity of the experiment with the SLS build process compared to previous imaging presented in Chapter 2. The resulting images showed the crystalline spherulites to be a strong source of scattering in the resolidified part. Discussion into the significance of these results on the use of OCT in SLS is also provided. This paper is refined and expanded from work published previously in a peer reviewed journal article and peer reviewed conference paper [26,27].

3.2 Materials and Methods

3.2.1 Nylon Part and Ethyl Cinnamate

All of the powder imaged in this paper was commercially available, virgin PA650 (nylon 12) from Advanced Laser Materials (ALM). The data sheet provided by ALM gives a particle size range, D10-D90, of 30 to 100μm and a mean particle diameter of 55μm. The melting temperature is reported at 181°C.

The nylon part imaged was built on the Laser Additive Manufacturing Pilot System (LAMPS) at UT Austin. Details of the LAMPS machine can be found in Fish et alia [15]. The SLS part was designed to contain portions ranging from a single layer to 10 layers in thickness with each layer being nominally 100μm thick as shown in Figure 17. Typically,

the outside of an SLS part is covered in powder particles sintered to the outside of the melted region [2]. As shown in Chapter 2, powder particles were highly scattering which limited imaging depth. To improve imaging results for this study, the buildup of powder particles on the top surface of the part was prevented by cooling the part immediately after sintering the last part layer without covering the top layer of the part with any powder layers as is typically done in SLS.

The nylon powder and part were imaged in air as well as ethyl cinnamate. The ethyl cinnamate had a 98% assay, a reported index of refraction of 1.558, and was obtained from Sigma Aldrich [28].

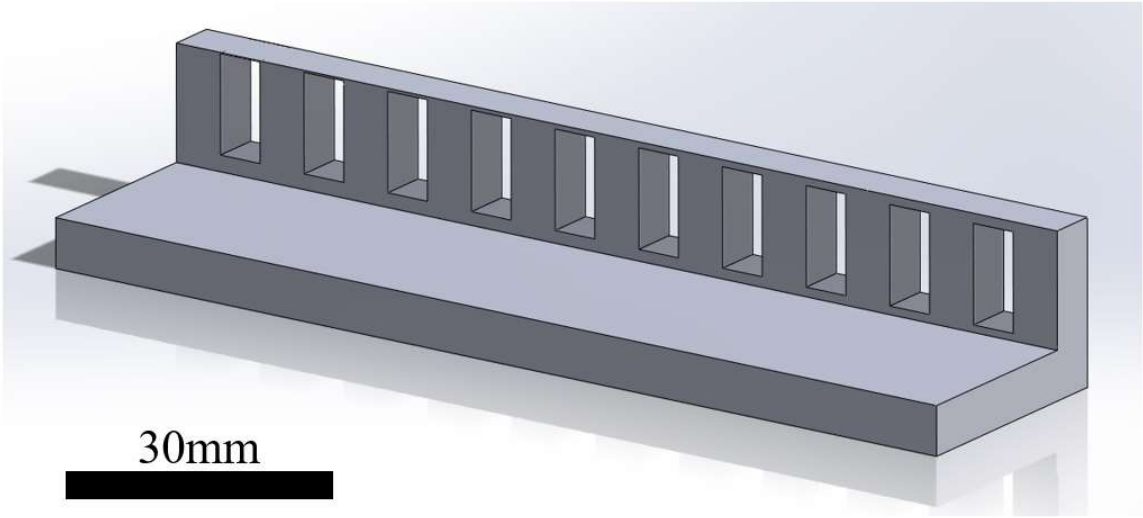

Figure 17: CAD of the SLS Nylon 12 Part Imaged. The thickness of the bridge-like areas increased from 100μm (left) to 1000μm (right) in thickness.

3.2.2 OCT Systems

In this work, two different commercially available Fourier domain, swept source OCT (SS-OCT) sources were used in different optical systems were used which will be referred to as Systems B and C to differentiate them from OCT System A that was used for the study in Chapter 2. Although the details of the systems vary as described below, they shared a common scheme design scheme with OCT System A given in Figure 7.

System B comprised of a commercially available AXSUN swept source laser with details given in Table 2. System B also contained a nanosecond pulsed thulium fiber laser (Nufern, SUB-1337) which could be used to radiate a sample while imaging. The thulium fiber laser operated at a wavelength of 1940nm, with a maximum average power of 15W. It emitted 100ns duration pulses with a maximum pulse energy of 500μJ. The axial spatial and pixel resolutions as well as the lateral pixel resolution were determined similarly to System A; however, the lateral spatial resolution was determined experimentally as described below.

A custom in-house-designed fast detection scheme using an InGaAs (G12182-003K, Hamamatsu) detector was used to record the intensity profile of the focused OCT beam at the back focal plane of the 25mm focal length scanning lens (AR112-ZC-XWL-25-25, ISP Optics Inc.) via use of precision mechanical stages (ATS100-150-u-20p, Aerotech Inc.) and placing the detector just behind a 2μm diameter pin hole (P2S, Thorlabs Inc.). The x,y,z-stages were positioned carefully to obtain the optimal spot of the highest intensity and the spot size was estimated along one axis by translating the pinhole using the precision mechanical stage. The recorded lateral beam profile gave a FWHM lateral

resolution of 20±2μm when using a 4mm collimator. Using a similar procedure, the spot size of the thulium laser was found to be 34±2μm.

Table 2: Key Parameters for OCT System B

Swept Source Laser Parameters			
Average Output Power	30 mW	Sweep Rate	100 kHz
Central Wavelength	1310 nm	Wavelength Tuning Range	100 nm
Resolution Parameters			
Axial Spatial Resolution	12±4 μm	Lateral Spatial Resolution (with 4mm collimator)	20±2 μm
Axial Pixel Resolution	8.6 μm/pixel	Lateral Pixel Resolution	varied

Three collimators (RC04, RC08 and RC12, Thorlabs Inc.) were used with OCT system B with beam diameters of 4, 8, and 12 mm resulting in various spot sizes. The spot size and be extension the lateral resolution scale inversely with the collimator diameter used. Changing the collimated beam diameter necessarily changes the Rayleigh length of the beam. The 4, 8, and 12 mm collimators caused Rayleigh ranges of around 240, 60, and 27μm respectively, which for the 8 and 12 mm collimators is less than the diameter of many of the powder particles. The small Rayleigh lengths result in a limited range where the B-scans are not highly blurred, but useful images were obtained despite this limitation.

System C also comprised of a commercially available AXSUN swept source laser with details given in Table 3. The axial spatial and pixel resolutions as well as the lateral

pixel resolution were determined similarly to System A; the lateral spatial resolution was determined experimentally as described for System B. The collimator used for the sample arm was RC04 (Thorlabs Inc.).

Table 3: Key Parameters for OCT System C

Swept Source Laser Parameters			
Average Output Power	30 mW	Sweep Rate	100 kHz
Central Wavelength	1310 nm	Wavelength Tuning Range	135 nm
Resolution Parameters			
Axial Spatial Resolution	12±4 μm	Lateral Spatial Resolution	15±2 μm
Axial Pixel Resolution	7.5 μm/pixel	Lateral Pixel Resolution	varied

3.3 RESULTS/DISCUSSION

3.3.1 Introduction

The OCT Systems were used to image nylon powder and parts in air and ethyl cinnamate at a room temperature of approximately 25°C. Nylon powder was also imaged while being sintered with the thulium laser. Each is discussed in the following sections.

3.3.2 Determining if Internal Multiple-Scattering and Reflections Contribute to Signal-Tail Artifact by Imaging Individual Nylon Particles on Mirror with OCT System B

To determine if the signal-tail was caused exclusively by inter-particle multiple scattering or if internal scattering and reflections contributed, individual PA650 particles were imaged on a mirror using OCT System B. Figure 18 shows an en-face OCT image of three powder particles. The cross-sectional view of the top particle is shown in the bottom three images using various intensity-to-grayscale color maps in order to highlight different features. In the bottom left image, only the highly reflecting mirror surface was visible. The mirror surface appears to curve beneath the powder particle due to the index of refraction mismatch of the powder and air. A signal-tail starting at the particle and extending down below the mirror surface can be seen in the bottom right image. The lack of proximity of other powder particles indicated that this signal-tail was caused by internal scattering and/or reflections. This experiment shows that in general, the signal-tail may be caused by both interparticle and intraparticle multiple-scattering and reflections. Additionally, Figure 18 also shows the semicrystalline structures within the particle cause the light to scatter throughout the powder particle as opposed to only at the air/particle interfaces.

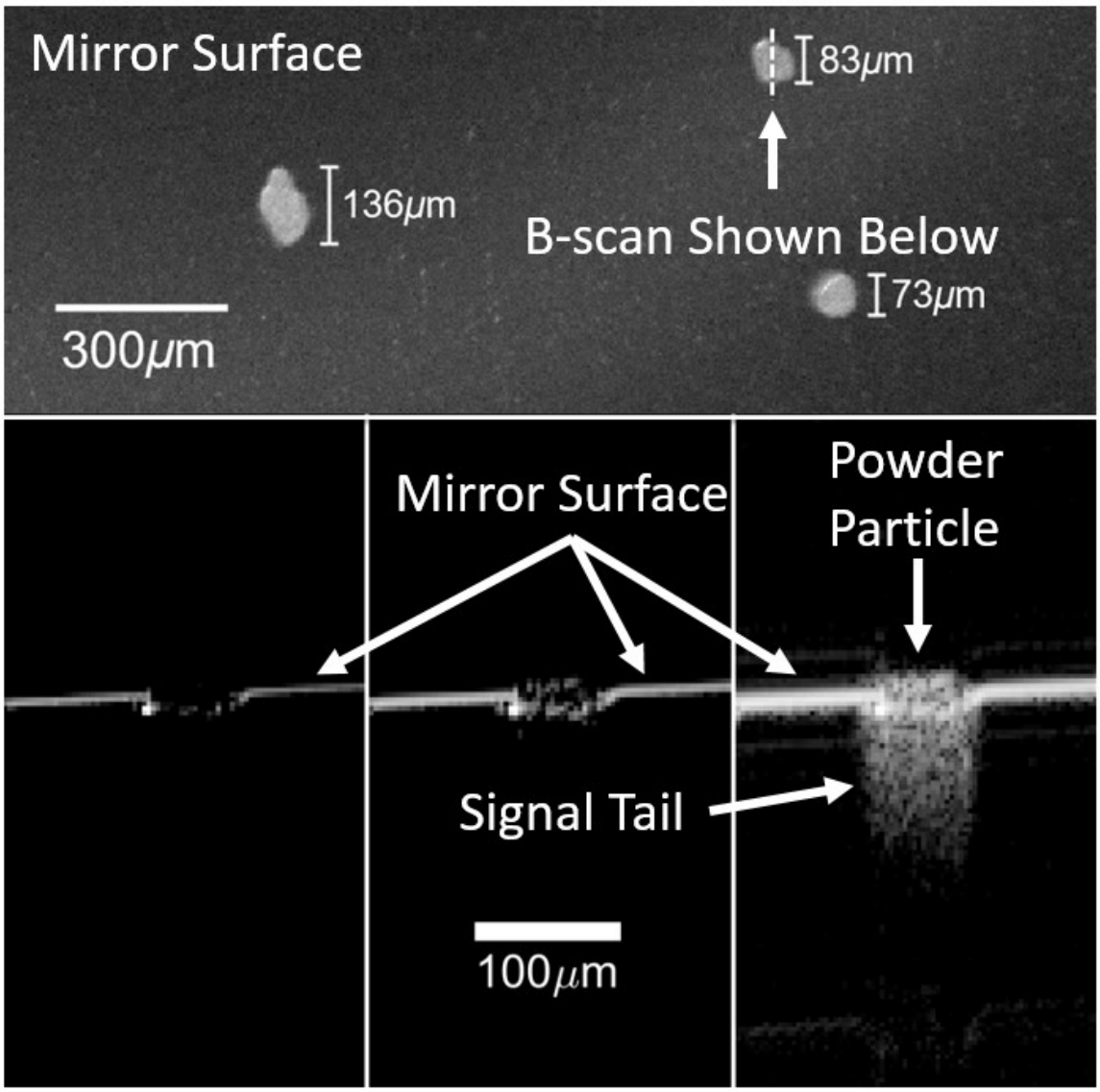

Figure 18: (Top) An en-face image of three powder particles on a mirror (Bottom) Three B-scans of the same OCT particle are shown with different intensity to grayscale mappings are presented (Bottom Left) The mirror surface is visible and appears curved beneath the powder particle due to the index of refraction mismatch between the air and the particle (Bottom Center) The powder particle begins to come into view. (Bottom Right) The powder particle is in view as well as a signal-tail artifact extending ≈100μm below the particle.

3.3.3 Confirming Multiple Scattering/Reflections as Cause of Signal-Tail Artifact by Imaging Nylon Powder in Ethyl Cinnamate with OCT System B

Multiple-scattering was further confirmed as the cause of the signal-tail artifact by imaging a nylon powder bed in ethyl cinnamate. The ethyl cinnamate had a reported index of refraction of 1.558 which nearly matched the nylon 12 index of refraction of 1.53. By immersing the powder particles in an index matching liquid, both the internal and interparticle multiple-scattering events were reduced sufficiently to eliminate the multiple-scattering imaging artifact seen when the powder/air samples were imaged. The imaging depth of nylon in ethyl cinnamate was then determined to document the improvement when immersed in an index-matched liquid. One hundred B-scans were averaged together to improve the signal-to-noise ratio (SNR). The resulting image of nylon powder in ethyl cinnamate is shown in Figure 19. The index-matched liquid eliminated the signal-tail as expected allowing the individual particles as well as the liquid regions between the particles near the top of the sample to be differentiated. The imaging range (6 dB above background) of nylon powder in ethyl cinnamate is 499μm, a 15.4-fold improvement in imaging depth over the powder/air system (32.4μm). Although interparticle scattering was greatly reduced, scattering from within the powder particles was still visible in Figure 19 due to the spherulitic crystalline structures within the powder particles.

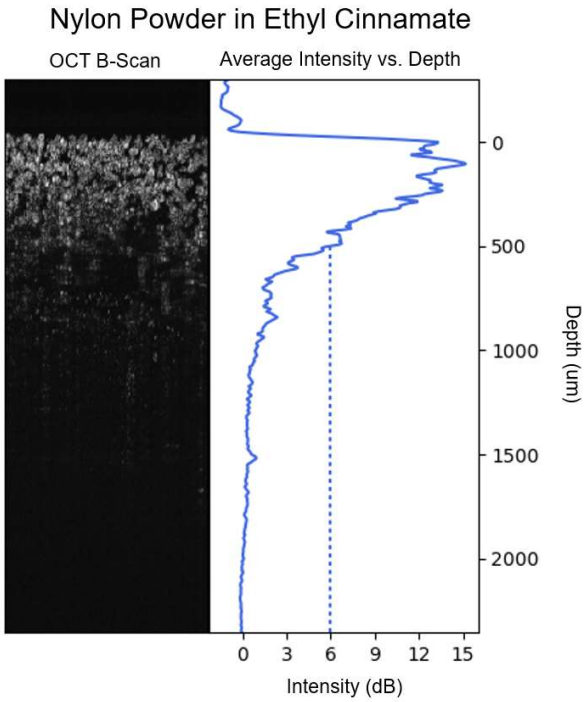

Figure 19: (Left) OCT B-scan of nylon powder in ethyl cinnamate (Right) The average intensity of the OCT A-scans is shown vs. depth. The imaging depth (6dB above background) of nylon 12 powder in ethyl cinnamate is 499μm.

3.3.4 Quantifying Contrast Improvement of SLS Nylon Components when Imaging in Index-Matched Media with OCT System C

To test if a similar improvement in imaging would occur for finished nylon parts, the SLS nylon part with varying thickness bridge-like structures (Figure 17) was imaged in both air and ethyl cinnamate. During imaging, a volumetric scan of each of the bridge-like sections of varying layer thicknesses was first taken. Afterwards, the part was placed in a container and covered with ethyl cinnamate. The part was weighted down to prevent it from floating. The volumetric scans were repeated under the new conditions. The plane

of best focus was set to be the top of the part prior to collecting each volumetric scan to enable useful image comparison. After collection, several of the volumetric data sets were aligned manually using the FIJI distribution of ImageJ [29,30]. The aligned images are shown in Figure 20. Review of the aligned images revealed several notable differences in the air and ethyl cinnamate systems. First, the top surface of the nylon part was brighter in the air images than in the ethyl cinnamate images because the index-matched media eliminated the majority of the reflections from the part surface resulting in increased contrast within the part. In order to quantify this effect, the contrast to noise ratio (CNR) was calculated for each image as commonly defined by other researchers [31–34]:

$$CNR = \frac{f - b}{\sqrt{\sigma_f^2 + \sigma_b^2}} \tag{1}$$

where f and b are the mean grey values of foreground and background respectively, and σ_f and σ_b are the respective standard deviations. An area near the top of the SLS part was manually chosen for the foreground area in Equation 1 to ensure the foreground regions used were within the Rayleigh range of the OCT system (≈300μm). A background region of the same size was selected just above the part. The specific areas chosen are indicated by the white rectangular outlines in Figure 20. The CNR values are given in Table 4.

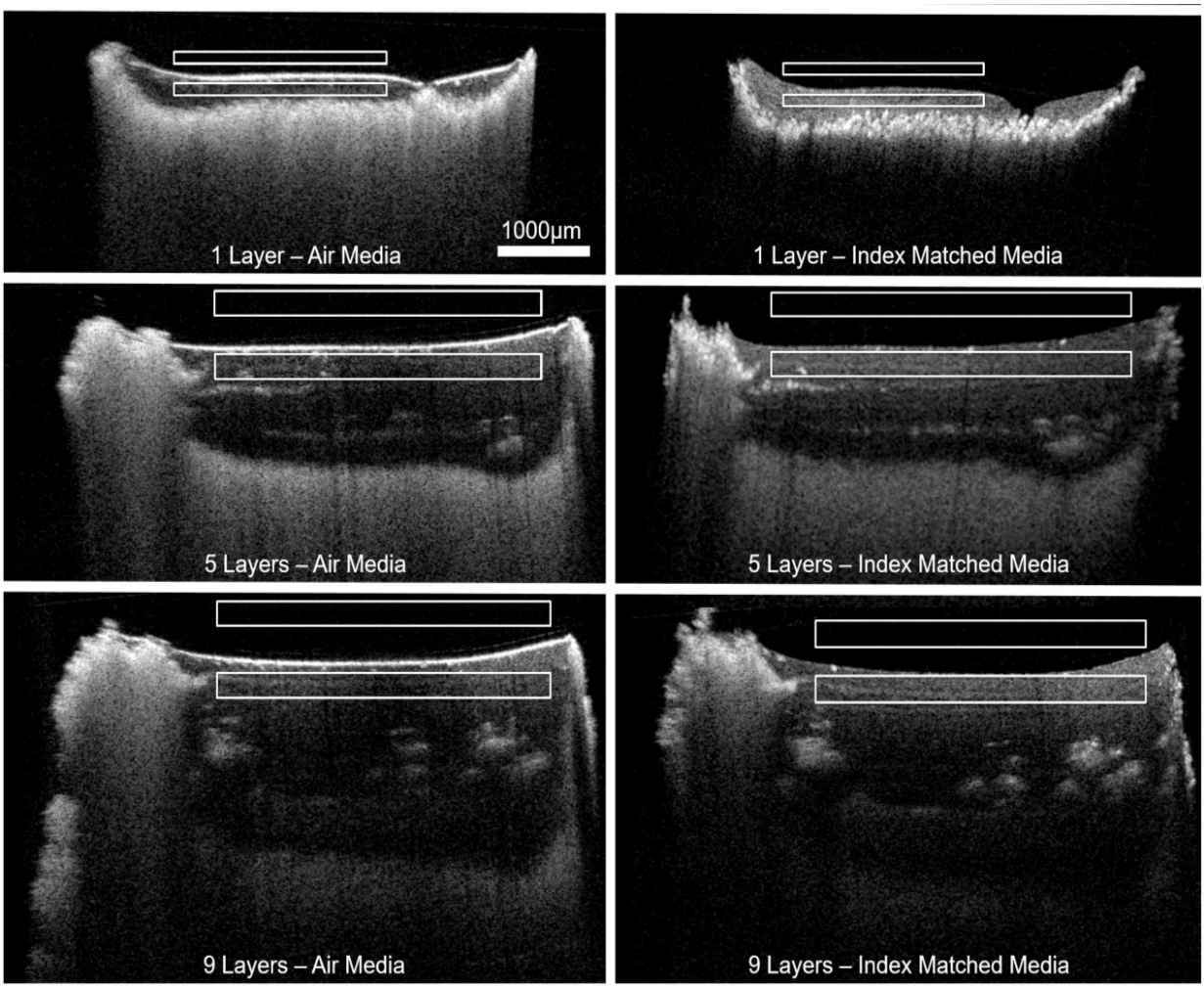

Figure 20: Nylon 12 SLS Part of varying thicknesses in air and an index matched liquid. Rectangular regions used in the CNR calculation are outlined in white.

3.3.5 Confirming Nylon Spherulites as Source of Internal Scattering in SLS Nylon Powder by Imaging Nylon Powder in Cuvette with Concurrent Melting with OCT System B

To confirm that the nylon spherulites were the source of the internal scattering seen in the nylon particles in Figure 18, powder was imaged concurrently during melting and

resolidifcation. The nylon powder was imaged inside a cuvette while a portion of the nylon powder was melted from the side with a thulium laser as shown in Figure 21. The OCT laser began imaging after which the thulium laser was turned on for a fraction of a second and the OCT laser imaged for the next few seconds to capture the melting and resolidification of the nylon powder. Several of the captured images appear in Figure 22.

Table 4: CNR Improvement when Imaging SLS Part in Ethyl Cinnamate (EC)

No. of Layers Being Imaged	Media	CNR	CNR Improvement in EC (dB)
1	EC	4.08	3.45
1	Air	2.74	
5	EC	3.37	3.49
5	Air	2.25	
9	EC	3.59	4.60
9	Air	2.11	

Figure 22a shows the powder before the thulium laser was turned on. The powder surface appeared with a brightly reflecting surface and a signal-tail as seen previously. Figure 22b shows the powder after the thulium laser began to heat the powder. The powder had shifted slightly, and the signal-tail appeared to shimmer and shorten as the powder melted and became more transparent. Figure 22c shows the agitating, transparent melt region. Several brightly reflecting powder particles were still visible. Figure 22d was

captured a few seconds later after the transparent, melted region had stopped. Pores and perhaps some unmelted particles appeared to be present in the melted region. After this, Figure 22e shows the transparent region becoming more opaque starting from the surface of the melted region, and Figure 22f was taken after the opacity had stopped spreading.

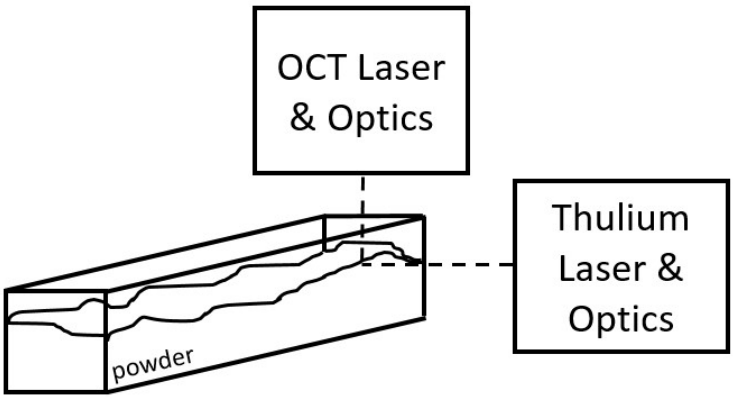

Figure 21: Schematic of setup for simultaneous imaging and melting of nylon 12 powder in a cuvett.

The powder particles were opaque, but became transparent when the spherulites melted as seen in Figure 22d. As the melted region cooled and spherulites reformed and solidified the melt in Figure 22e and Figure 22f, the opacity returned. This is consistent with opacity spreading from the surface of the melted region as it cooled since the surface of the melted region would be expected to reach the recrystallization temperatures first as the melted region cools. This is also consistent with the semicrystalline powder and sintered parts having been highly scattering while the high temperature melted region was more transparent as seen in this and other works [21–23].

3.3.6 Implications of Results on OCT use in SLS

The results shown in this paper have practical implications for the use of OCT for ex-situ optical non-destructive evaluation of nylon 12 parts and in-situ process monitoring of SLS. Powder was shown to have an imaging depth of 32.3μm while the typical layer thickness in SLS is ≈100μm.

When using OCT as an in-situ sensor, melted nylon is optically homogenous with high transmission of the OCT beam, but the limited imaging depth of nylon powder could prevent imaging of the melted nylon once it has been covered with even a single layer of nylon that is not melted on the subsequent layer. Since additive manufacturing is often used specifically for its ability to create highly complex, bespoke components, this limits the utility of OCT as a process sensor to image any but the top-most layer during the SLS process in general.

Powder was also shown to exhibit a signal-tail artifact which obscures the image beneath the powder. Unmelted powder often sinters to the edge of nylon parts as seen in the bottom of the parts in Fig. 9 and other works [2,3]. When using OCT for optical nondestructive evaluation, the signal-tail artifact from the outer powder layer has the potential to obscure imaging beneath it unless removed or imaged in an index-matched media.

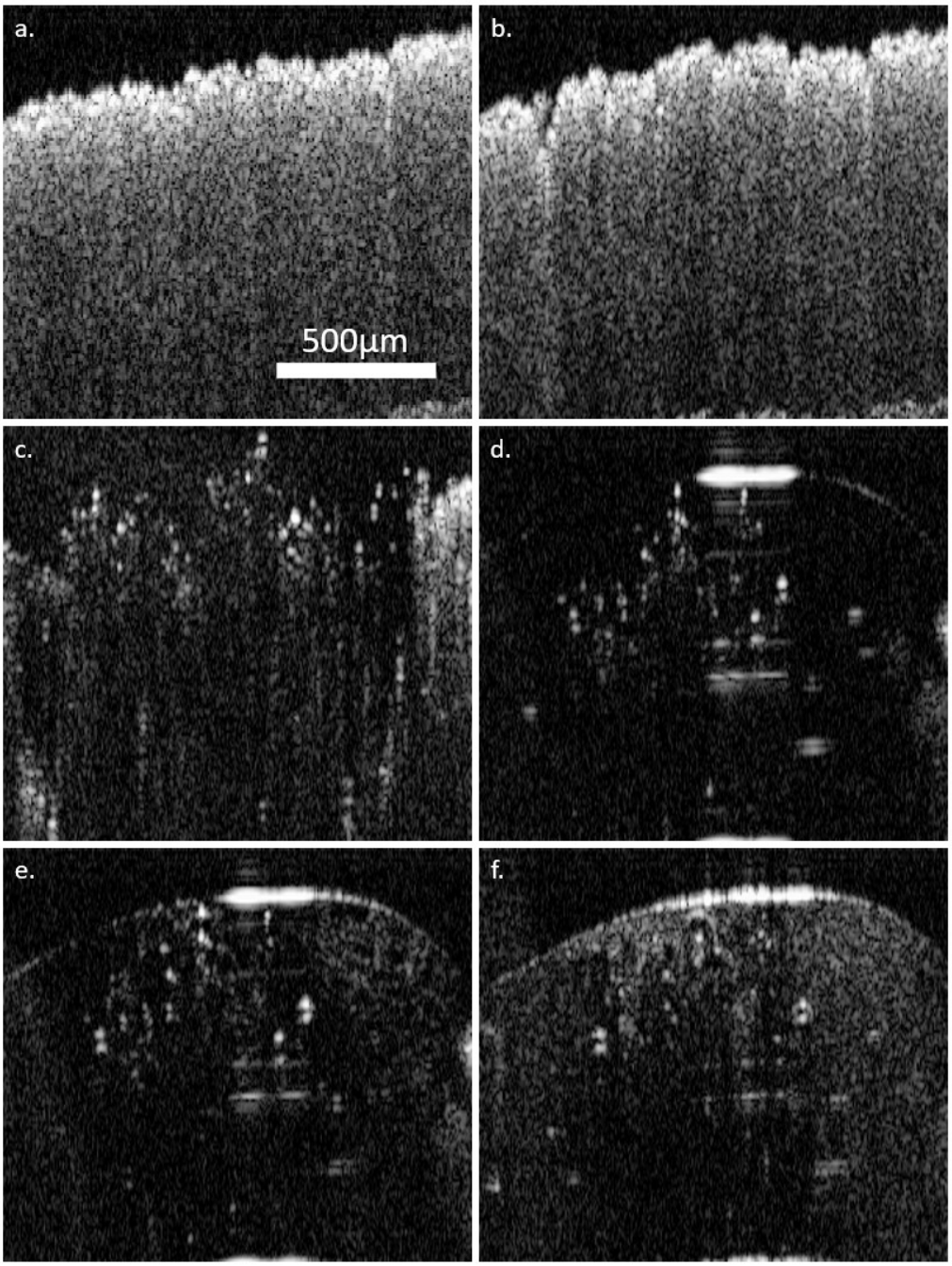

Figure 22: Nylon 12 powder at various stages of melting and resolidification. (a) Nylon powder before sintering had begun, (b) the powder shifted as it was heated by the thulium laser, (c) the agitating, transparent melted powder is shown, (d) the melt region after agitation had ceased, (e) the melt region turned opaque as it solidified, and (f) the melt region after resolidification was complete.

Imaging depth through powder was improved when the powder was immersed in an index-matched liquid. The SLS process will not function with the powder bed immersed in liquid without major modifications to the SLS process. Thus, the imaging improvement through nylon powder particles when immersed in an index-matched liquid is not useful to in-situ OCT imaging of the SLS process; however, this improvement may be useful when using OCT for nondestructive evaluation of SLS components. Contrast was shown to improve by as much as 4.6 dB (70%) when imaging samples in ethyl cinnamate rather than air in this paper.

The recognition that spherulites cause the transparent melted nylon to become more opaque to OCT as the nylon resolidifies suggests the use of OCT for in-situ sensing of solidification in the top layers of nylon parts. Controlling the thermal environment in SLS is known to be extremely important for dimensional accuracy and mechanical integrity [11], and premature resolidification could indicate a non-ideal thermal environment during the SLS build process, and warrants additional research.

3.4 Conclusions

In this chapter, multiple-scattering was shown to cause an imaging artifact which contributed to the limited imaging depth in nylon powder. Subsequent imaging of individual powder particles on a mirror as well bulk powder in an index-matched liquid confirmed that both interparticle and intraparticle multiple-scattering and reflections contribute to the artifact. Using ethyl cinnamate as the imaging media for nylon powder eliminated the imaging artifact and increased the imaging depth to 499μm. Sintered nylon

12 was then imaged in air and the index-matched liquid, and the contrast was improved by as much as 4.6dB (70%) when imaging in the index-matched media. Finally, nylon powder was continuously imaged before, during, and after melting and resolidification. The resulting images showed the opaque powder become uniform and transparent as the powder melted and subsequently the nylon became more opaque as the nylon recrystallized showing the crystalline spherulites to be a strong source of scattering in the resolidified SLS part. Finally limitations, imaging suggestions, and a future area of research regarding OCT use in SLS for optical nondestructive evaluation and in-situ SLS process sensing were given based on results in this paper.

Chapter 4: Integrating Optical Coherence Tomography on the LAMPS Machine

4.1 Introduction

In Chapter 2, OCT imaging of the SLS process was established to be feasible, and that the complete volume of the part is likely to be able to be imaged one layer at a time. Additionally, in Chapter 3, understanding of the cause and nature of scattering in the SLS nylon powder, melt, and resolidified parts was improved. Having done this, the next step was to integrate an OCT system with the LAMPS machine for in-situ data collection. This chapter describes the optical design of the integrated OCT/SLS system as well as the hardware and software implementation for improved noise reduction, correction of imaging artifacts, and improved ease of sectioning the data for visualization. This chapter was revised and expanded from the author's work published in a peer reviewed journal article [35].[3]

4.2 Optical Design

The SLS optical design (Figure 23) includes a CO_2 laser (collimated output with a beam diameter of 4.2 mm), a Keplarian telescope for beam expansion (1:5.9) and an objective lens (f=750 mm, NA=0.015) that focuses light onto the build surface. The beam

[3] This chapter contains work previously published in M.R. Gardner, A. Lewis, J. Park, A.B. McElroy, A.D. Estrada, S. Fish, J.J. Beaman, T.E. Milner, In situ process monitoring in selective laser sintering using optical coherence tomography, Optical Engineering. 57 (2018) 1. doi:10.1117/1.OE.57.4.041407. In that work, A.D. Lewis performed the primary experimental design and data collection and actively consulted with the other researchers regarding the analysis performed.

is directed by a pair of post-objective scanning galvanometers and enters the build chamber through a zinc selenide (ZnSe) window. The maximum area build surface is a circle with radius 109 mm; the radius of the build area is constrained by the size of the ZnSe window.

The OCT system (Figure 23) is a fiber-based Mach-Zender interferometer design with a swept source laser (central wavelength = 1310 nm, Axsun). The sample arm light is collimated to a 12 mm diameter by a reflective collimator and focused by a long focal-length objective lens (f=750 mm, NA=0.008). The OCT beam is co-aligned with the sintering beam using a dichroic mirror and is scanned by the same post-objective scanning galvanometers before the light enters the build chamber through the germanium window. Thus, the OCT beam and CO_2 beam are always incident on the same location. The peak sensitivity of the system was experimentally determined to be 98.6 dB with an axial resolution of 11.7 um. The system roll-off yielded an imaging range of 3.36 mm (Figure 25).

Figure 24 shows a picture of the physical hardware used for the co-alignment of the OCT and CO_2 lasers. Although ZnSe is the standard window material used in SLS machines, it is not ideal for use with both OCT and CO_2 lasers passing through it due to attenuation of both beams. To reduce attenuation of both beams, a potassium chloride (KCl) window was used at times in the LAMPS machine which reduced attenuation significantly. However, the potassium chloride window was hygroscopic and deteriorated over time. To increase the life of the KCl windows, they were stored in a desiccator when not in use.

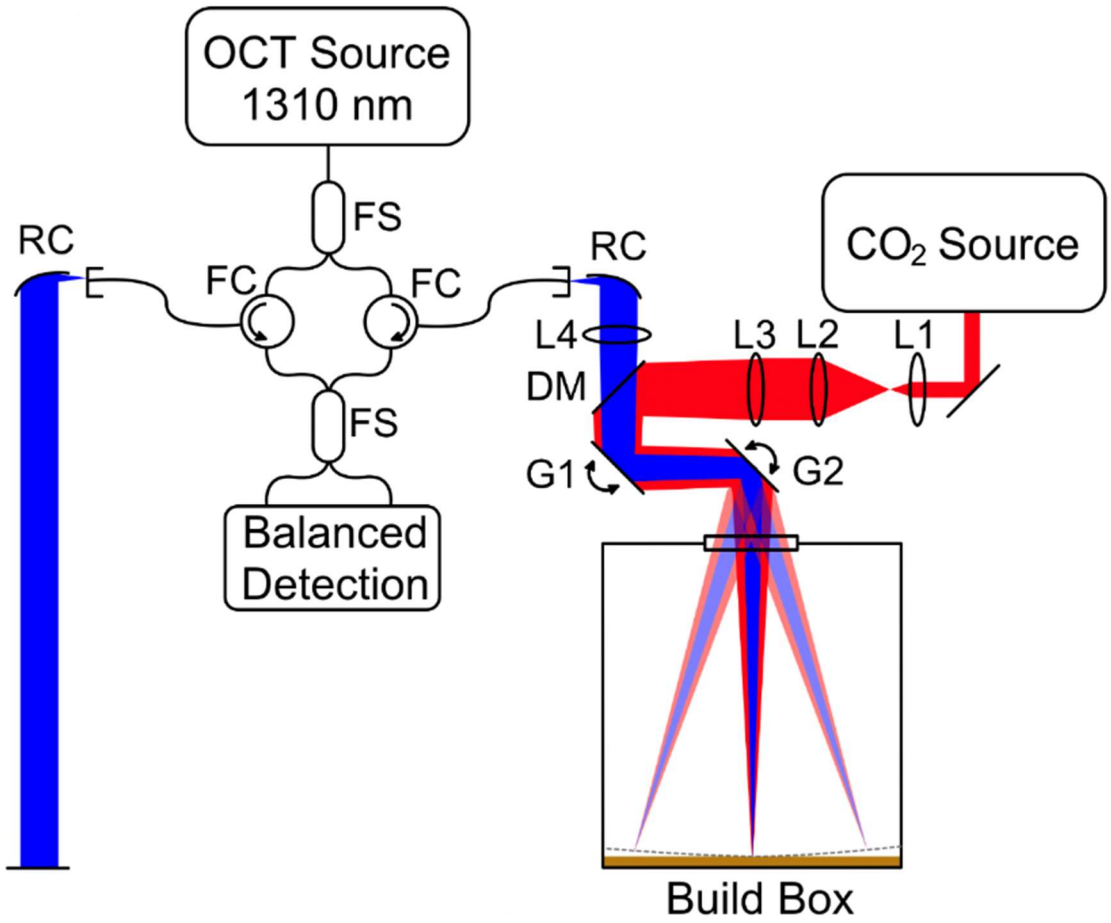

Figure 23 The SLS+OCT system combines a CO2 sintering laser (red) with an OCT imaging system (blue). Lens 1 (L1) and lens 2 (L2) are a telescopic beam expander, and lens 3 (L3) is the sintering laser [1]

84.2.2 False Curvature

One consequence of the presented design is that the OCT beam path length is greater towards the sides of the build surface than it is at the center. This causes a hyperbolic distortion in the apparent surface of the build area with areas farther from the center of the build surface appearing lower than areas near the center of the build surface

as illustrated in Figure 26. Additionally, the OCT beam's large focal length lens, though necessary to position the optics in the laser box, yields a diffraction limited spot size of approximately 186 μm. The large spot size and variation in the sample produce a reduced signal amplitude. Also, the large focal length results in a reduced solid angle of the captured back reflected radiation. Both of these effects lead to a reduced signal to noise ratio (SNR).

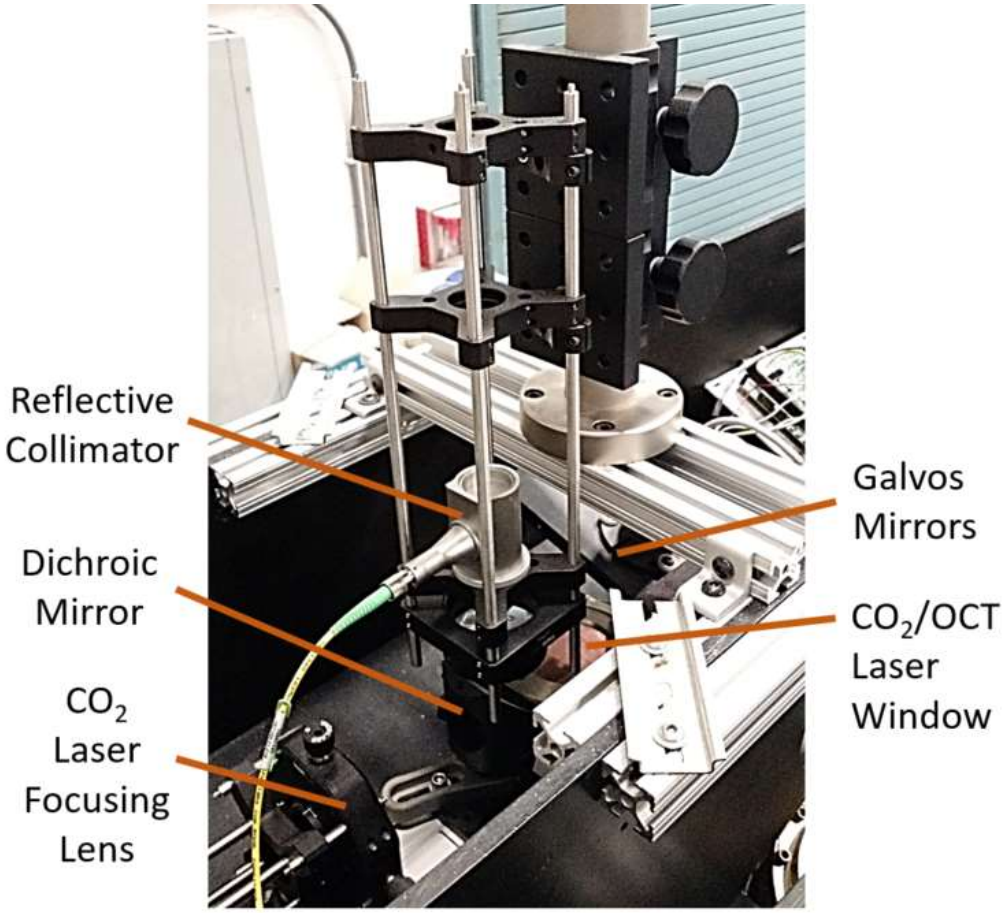

Figure 24: Image of the hardware inside the LAMPS laser cabinet that is involved in co-alignment of the OCT and CO2 beams. The OCT beam travels through the fiber optic cable, is redirected by the reflective collimator, and is co-aligned with the CO2 at the dichroic mirror. The two beams reflect of the mirror galvanometers (galvos) through the Zinc Selenide window and onto the surface of the build box inside the LAMPS machine.

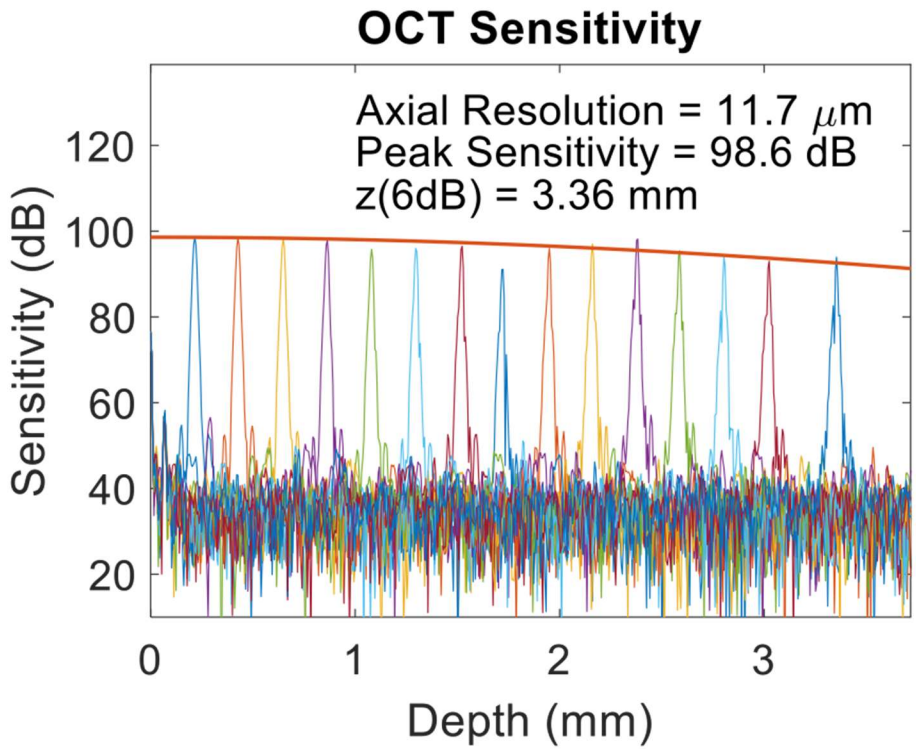

Figure 25 The OCT system was experimentally determined to have a peak sensitivity of 98.6 dB and an axial resolution of 11.7 μm. By fitting a Gaussian curve to the peak sensitivities at increasing pathlengths, the imaging range (6 dB) was calculated to be 3.36 mm [35]

4.3 Additional Features

Additional work was necessary in order to improve the utility of the data from the OCT/SLS system. First, the OCT data was registered with the position on the build surface where the data was taken. This allowed for automatic sectioning of the OCT data for improved data visualization, greatly increasing the speed of future data analysis. Correction for the artificial curvature mentioned in Section 4.2.2 above was also implemented. Finally, constant background noise was also subtracted and an interleaving

technique was used to further improve image quality. These techniques were developed and implemented over time so some of the data presented in coming chapters may make use of some, all, or none of these improvements according to what had been implemented at the time of analysis.

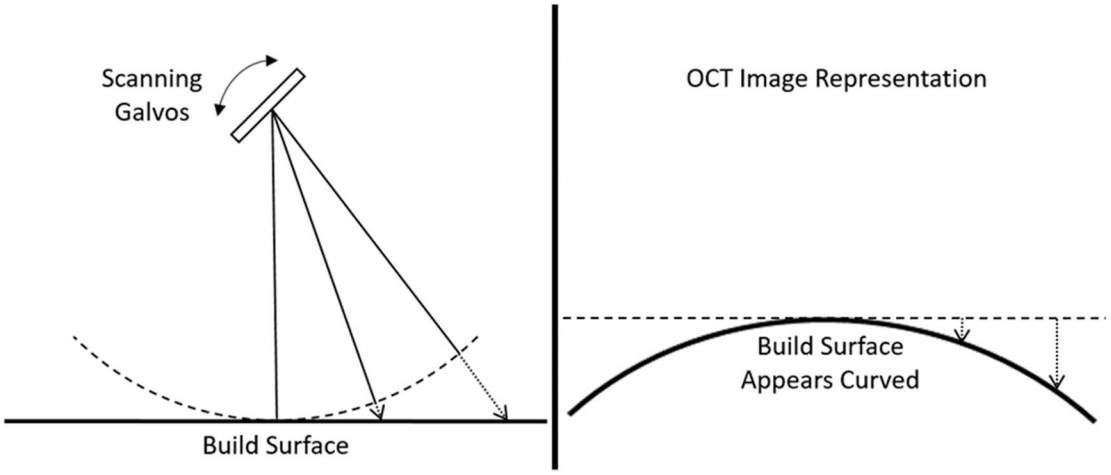

Figure 26: (Left) When imaging farther from the center of the build surface, the path length of the light is greater. (Right) This causes the flat build surface to appear hyperbolically curved in the OCT image because the height in the OCT image is determined by the optical path length of the beam

4.3.1 Registration of OCT Data with Position

The OCT sensor had the potential to be used to collect 3d and 4d datasets of the parts being built in the SLS machine, but doing so required registering the OCT data to the location where it was collected. In order to accomplish this, position was collected with the laser galvanometers which direct the OCT and CO_2 lasers.

The galvanometer on the LAMPS machine was made by Cambridge Technology and included a capacitive feedback system linked to a galvo controller, a digital to analog

converter, two MiniSAX servo controllers (one for each axis of motion) and the mirrors themselves. The galvo controller contains ports to read the position of the galvanometer mirrors. The position signals were routed to the Galvo DAQ device which was a BNC-2110 Shielded Connector Block Assembly made by National Instruments. The Galvo DAQ was triggered to record the galvanometers' positions by the trigger from the OCT Laser which was routed through the OCT DAQ. The OCT DAQ device was the ATS9350 – 12 bit, 500 MS/s waveform digitizer board from AlazarTech. The clock and trigger from the OCT laser were both routed to the OCT DAQ. The laser beam itself was directed through the interferometer and sample being imaged as shown in Figure 23. The detected signal was also then routed to the OCT DAQ. From there, the digitized galvanometers' positions and the digitized raw OCT data are then transferred to the computer from their respective DAQ devices. The operating software for the integrated OCT/LAMPS machine was written in LabVIEW 2016. The frequency domain OCT data is then converted to the time domain via a fast fourier transform on the computer, the galvo voltage is correlated to position, and additional post processing could be performed as desired. This communication flow is shown in Figure 27.

4.3.2 Automatic Sectioning of OCT

Once each A-scan had an associated build surface position coordinate associated with it, the data needed to be sectioned and arranged spatially to improve data visualization and interpretation. To accomplish this in an automated way, the scans to be sectioned were limited to a bidirectional raster scan pattern as shown in Figure 28. The imaging included

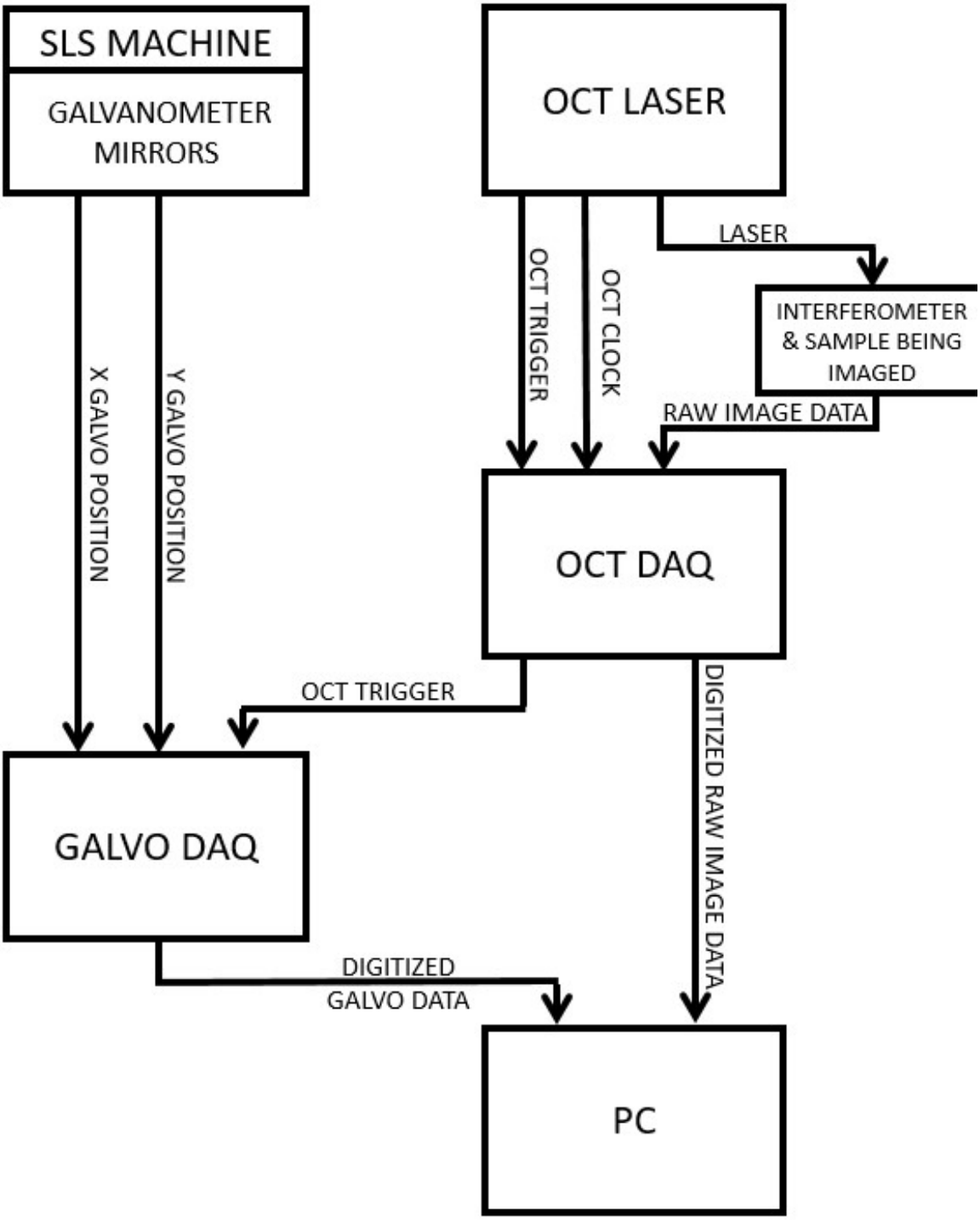

Figure 27: Diagram of the hardware communication utilized to synchronize the OCT laser with the position at which it was collected.

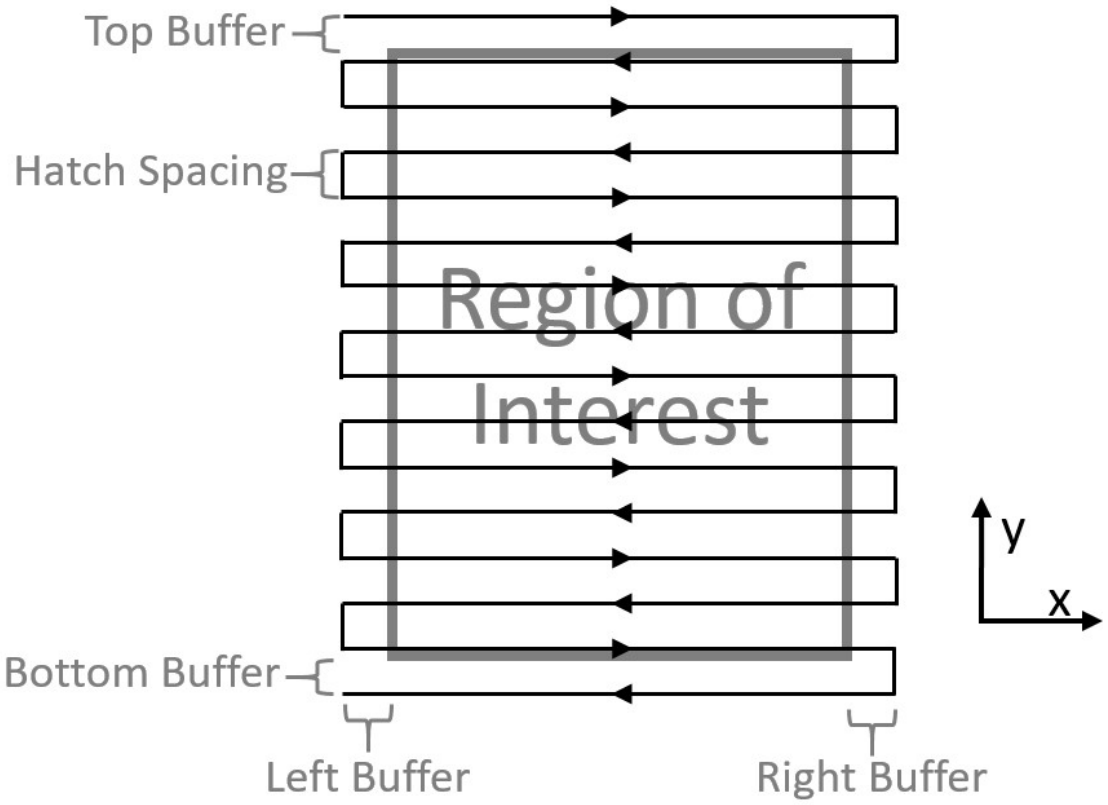

Figure 28: An example of a bidirectional raster imaging scan on a region of interest is shown. Buffers around the region of interest help account for galvanometer acceleration/deceleration and misalignment of the OCT and CO2 beams.

a small buffer area on each side of the region of interest. The side buffers were typically about 2 mm and allowed the galvanometer mirrors to accelerate and decelerate to and from the scan speed without distorting the collected images in the region of interest. Without this buffer, the collected images appear slightly stretched where the galvos are accelerating/decelerating due to their slower than nominal speed in those areas. The top and bottom buffers were used to ensure the region of interest was imaged even if some misalignment between the OCT and CO_2 lasers was present.

A typical x-axis galvanometer signal from a bidirectional scan pattern can be seen in Figure 29a. The portion of the signal shown in Figure 29a shows 3 scanlines, the first and third going left to right, and the second travelling right to left. Figure 29b shows a magnified view of the area in the black square in Figure 29a. It shows the effect of interference from the stepper motors which control the piston and the hopper rotation motion in the LAMPS machine. When the stepper motors were de-energized, the interference ceased as well. Because de-energizing the motors while imaging would slow down the build process, and possibly allow the piston to wander from its position, software filtering was instead used to clean the galvos signal. As shown in Figure 29b, the interference resulted in deviations in which a single position reading was far from its "true" value, but would return to a more reasonable value on the very next position reading. Therefore, the first filtering step was deleting each point that was greater than a certain threshold away from its neighboring points. Afterwards, a 5^{th} order Butterworth filter was applied to further smooth the data. The resulting fit is shown in Figure 29c.

After the filtering was performed, the contiguous indices of the galvo sample with a position lying within the coordinates of the region of interest were identified as the individual scanlines as shown in red in Figure 29d. After identifying the indices corresponding to each scanline, it was found that due to small variations in the speed of the galvo on successive scanlines, some scanlines consisted of more position data points than others. Given that most image visualization software is built to portray non-jagged 2D and 3D image datasets, the next step was to adjust the set of scanlines so that each scanline consisted of the same number of galvo position data points.

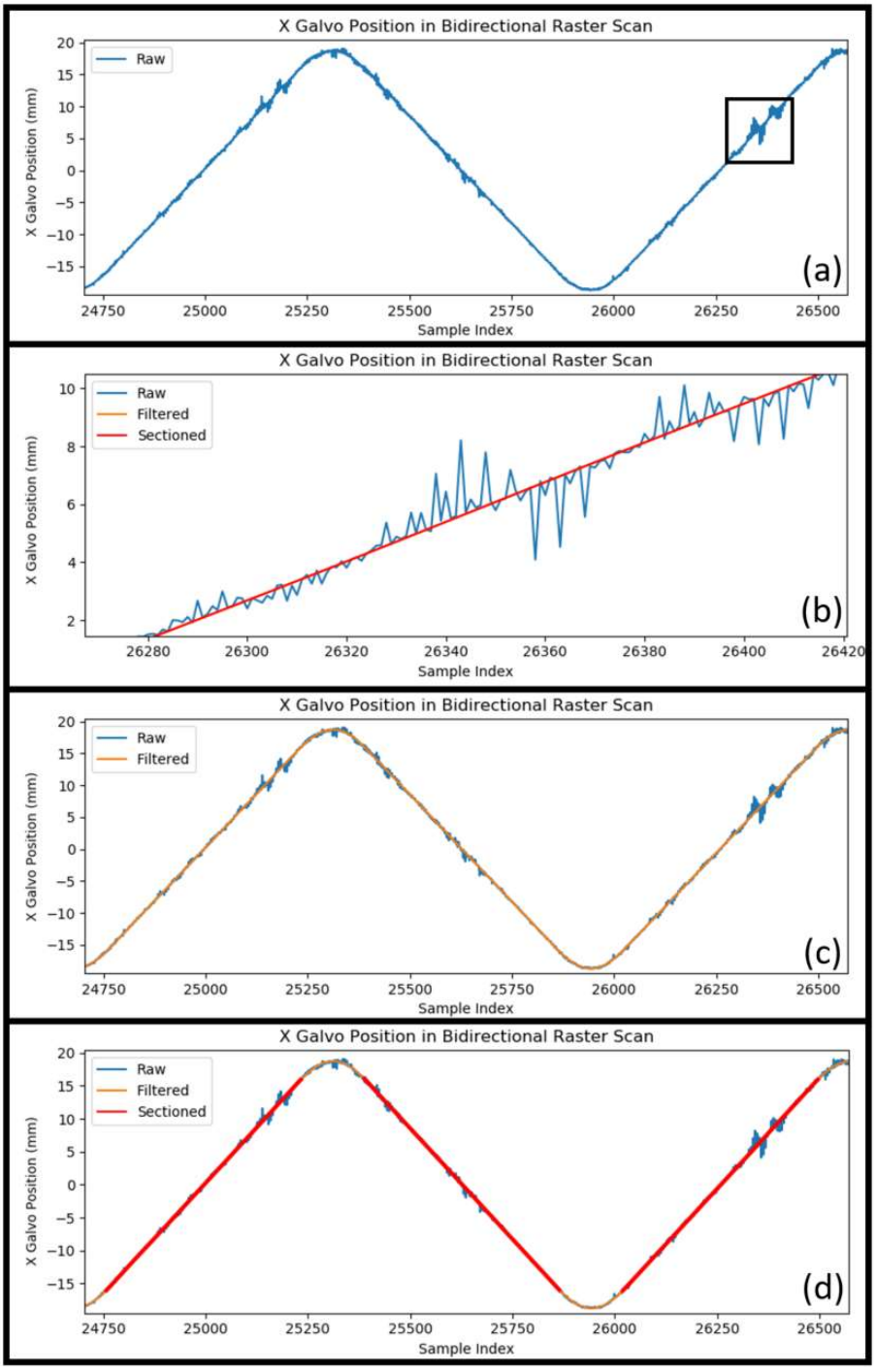

Figure 29: (a) raw galvo signal (b) zoomed in section of raw galvo signal showing noise (c) signal after signal filtering (d) the sectioned galvo signal is shown in red.

To do this, the scanline with the most position data points was used as a pattern. Then every other scanline (called cloth scanlines) was sectioned so that the x positions of the cloth and pattern matched as closely as possible. The x positions of the cloth and pattern were matched up in the following manner. For every point in the pattern scanline, choose the data in the cloth scanline that was taken at the closest x position to that pattern data point, then put that cloth data in the same scanline index position as the pattern data point to build the sectioned cloth scanline. An example is shown in Figure 30.

Figure 30a shows an example scanline from an OCT imaging dataset in which the scanline ran from -5mm to 5mm on the build surface. Each data point in each scanline consists of a scanline index, the x galvo position, the y galvo position (not shown), and the OCT A-scan collected at that position (shown here as a series of random unsigned 16-bit integers). Figure 30b shows an example non-sectioned cloth scanline with fewer indices than the pattern scanline. Figure 30c shows the cloth scanline after being sectioned. After sectioning, each data point in the sectioned scanline is the closest (in terms of x position) point in the cloth scanline to the pattern scanline data point at the same index. As seen in Figure 30b-c, this algorithm could remove data at times though this didn't seem to be a problem during the use described in this work. The data point in Figure 30b at index 2 was not carried into the sectioned scanline because it wasn't the closest point in the non-sectioned cloth scanline to any of the data points in the pattern scanline. The result of sectioning is shown in Figure 30d where the sectioned scanline is more closely aligned with the pattern scanline than the non-sectioned scanline. It should be noted that this

Pattern Scanline

Scanline Index	0	1	2	3	4	5	6	7	8	9	10
x position	-5	-4	-3	-2	-1	0	1	2	3	4	5
A-Scan Index	----------				-OCT Data Below-						
0	52674	15768	7687	64000	27451	63825	43967	62934	56777	62567	65234
1	3699	14635	64090	49077	27862	49961	23291	13572	41072	50198	22775
...	...	...	...	...	...	...	...	...	...	...	...
2047	10746	9612	27970	21618	55887	26294	64015	61666	65013	13423	30350

(a)

Non-Sectioned Cloth Scanline

Scanline Index	0	1	2	3	4	5	6	7	8	9
x position	-5	-4.3	-3.6	-2.9	-1.4	0	1.4	2.8	4	5
A-Scan Index	----------				-OCT Data Below-					
0	6415	23299	20272	47648	18949	8342	15863	7023	37710	41746
1	17915	16300	37824	40625	35190	6062	3968	49561	55966	46541
...	...	...	...	...	...	...	...	...	...	...
2047	26430	56641	53221	25787	41868	783	4423	22665	18225	10895

(b)

Sectioning Process

Sectioned Cloth Scanline

Scanline Index	0	1	2	3	4	5	6	7	8	9	10
x position	-5	-4.3	-2.9	-1.4	-1.4	0	1.4	1.4	2.8	4	5
A-Scan Index	----------				-OCT Data Below-						
0	6415	23299	47648	18949	18949	8342	15863	15863	7023	37710	41746
1	17915	16300	40625	35190	35190	6062	3968	3968	49561	55966	46541
...	...	...	...	...	...	...	...	...	...	...	...
2047	26430	56641	25787	41868	41868	783	4423	4423	22665	18225	10895

(c)

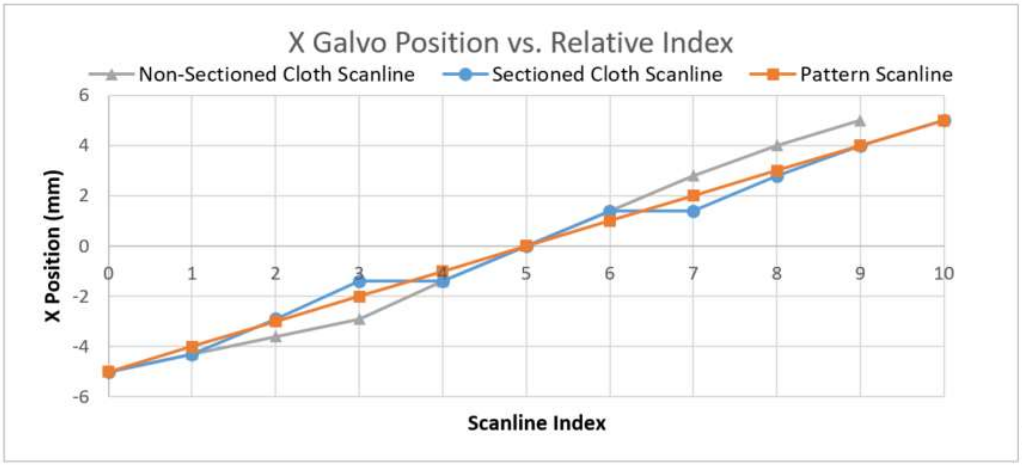

(d)

Figure 30: Example of the sectioning process yielding better aligned and non-jagged data.

example is for illustrative purposes only, and that in actuality, the data points collected were much more closely spaced than the ≈1mm shown in this example.

After each scanline had been sectioned so that all scanlines contained the same number of data points, the OCT data was transformed with the fast fourier transform and visualized using in-house software written in LabVIEW as well as in the FIJI distribution of ImageJ [29,30]. The sectioning process was performed each time the data was visualized.

4.3.3 Curvature Correction

As shown in Figure 26 and Figure 31, the design of the integrated OCT/SLS system resulted in a false hyperbolic curvature of the sample being measured. Assuming perfect alignment between the CO_2 and OCT beams, the hyperbolic curvature when imaging a level surface should take the form of Equation 3.

$$\frac{\left(z_{GTUI}+z_{OCT}\right)^2}{\left(z_{GTUI}+z_{OCT.min}\right)^2}-\frac{\left(x-h\right)^2}{\left(z_{GTUI}+z_{OCT.min}\right)^2}-\frac{\left(y-k\right)^2}{\left(z_{GTUI}+z_{OCT.min}\right)^2}=1 \quad (2)$$

$$z_{OCT}=-z_{GTUI}+\sqrt{\left(z_{GTUI}+z_{OCT.min}\right)^2+\left(x-h\right)^2+\left(y-k\right)^2} \quad (3)$$

In Equation 2, Z_{GTUI} is the distance from the galvos to where the unaliased OCT image would begin to appear and is a constant. Z_{OCT} is the distance from the top of the

OCT image to the level sample being imaged. X and y are the coordinates on the build surface that is being imaged. $Z_{OCT.min}$ is the minimum distance between the top of the OCT image and the level sample plane. Thus, $Z_{GTUI} + Z_{OCTmin}$ is the minimum distance between the galvos and the sample. H and k are the offset between the minimum distance point between the galvos and the sample and the origin of the build surface coordinates. Solving Equation 2 for Z_{OCT} and yields Equation 3.

After spreading a layer of powder with the LAMPS machine and collecting a scan of a portion of the powder bed, fitting a hyperboloid surface to the powder surface data was attempted. The error in the fit oscillated around the data, and it was unclear if the fit was not of the correct form perhaps due to imperfect alignment between the OCT and CO_2 beams on the galvo mirrors or if the powder was truly oscillating as the residuals indicated. In any case, an empirical correction was attempted afterwards.

In order to produce a flat surface, a container with liquid was placed in the LAMPS machine at room temperature. The flat surface of the liquid could be imaged with OCT and the true fit determined. Water and milk were used as the liquid, but the liquid/air interface did not produce a high enough signal. Heavy whipping cream was used thereafter and the higher fat content in the milk provided enough backscattering for a suitable signal. The surface data could then be captured and the same curvature could be subtracted out of subsequent data sets. This approach adds another step in order to correct the curvature, and must be redone anytime the OCT/CO_2 system alignment changes, or when the sample or reference arms are adjusted. For example, when the ZnSe and KCl windows were

exchanged in the sample arm of the LAMPS machine, the fit would change and need to be adjusted.

In practice, in order to get a reasonable surface correction with less effort, a 2nd order polynomial was fit to a scan of a large area of the powder bed, the fit was then applied to subsequent datasets to subtract the curvature. Then only relative changes from layer to layer were examined which were still reliable since the same curvature was used to correct each layer.

4.3.4 Noise Subtraction

It is common for images produced with OCT systems to have one or multiple erroneous horizontal lines across the image that do not correspond with an index mismatch in the sample. This is often caused by some piece of dust contacting one of the interfaces of the fiber optic components. In order to correct this defect, a common noise subtraction technique was performed. To accomplish this, before each bidirectional raster scan for OCT imaging, the laser was first commanded to the far top left corner, off the build surface where none of the OCT beam was coupling back into the interferometer within the coherence length of the OCT laser. This left a detected signal consisting solely of noise as well as the signal from the ghost lines. The mirrors were commanded to wait for 0.4 seconds and then the raster scan proceeded as normal.

This collection of the ghost line signal with each OCT scan allowed that data to be averaged (to minimize the noise) and then subtracted from every data point. This resulted in a significant reduction in the ghost line defect in the processed OCT images. An example

of the difference this noise subtraction could make is shown in Figure 31. Figure 31a and b show the same powder surface data, but Figure 31b has the noise reduction applied to the data. As indicated, the ghost lines are greatly reduced or eliminated after the noise reduction technique has been applied.

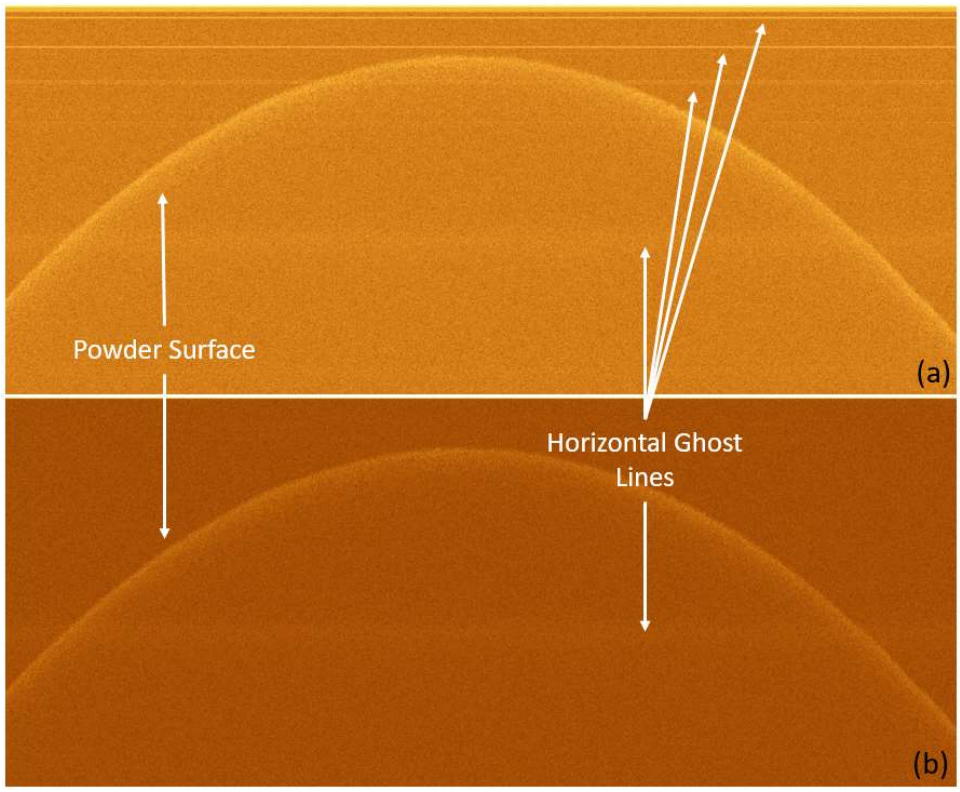

Figure 31: (a) shows a flat powder surface with several ghost lines running horizontally especially near the top of the image. (b) shows the same dataset but with noise subtraction.

It should be noted that as an alternative to the collection of the ghost line signal for each dataset, collecting a ghost line dataset at the beginning of an SLS build only was attempted. It was found, however, that the ghost line data would shift position slowly over

time, and the collected dataset would cease to eliminate the ghost lines after an hour or so. By taking a ghost line image with each scan, this obstacle was overcome.

4.3.5 Interleaving

On data sets with low penetration depths it was possible to further improve the image quality, a ”second-order interleaving” process could be used [35]. Using this image processing approach for OCT samples, every second data point in each A-scan fringe could be taken to form two A-scan fringes from the same A-scan location (1, 3, 5,..., 1375 and 2, 4, 6,..., 1376). The resulting two A-scans were averaged to improve SNR. Because the penetration depth of 1310 nm light in nylon powder was often less than half of the imaging range, the OCT signal from the build surface could be isolated to low-frequency fringe patterns. Thus, though the imaging range could be halved by second-order interleaving, and the build surface topology was maintained in both A-scans. Higher order interleaving was also possible and was performed on some data sets.

4.4 Conclusions

In this chapter, the optical design for an integrated OCT/SLS system was presented. Afterwards, several hardware and software features which played a role in data processing and visualization were discussed. Registration of OCT data with position data was accomplished by using the OCT Trigger to also trigger the position data collection. The OCT scans were limited to bidirectional raster scans enabling sectioning of scanlines and arrangement of the 3D data into a non-jagged data structure which could then be analyzed

with image visualization software. Several methods for curvature correction were discussed. A practical method to collect and subtract the background signal was explained. Finally, interleaving of raw data was discussed as a technique that could further be used to reduce the noise floor in OCT samples with small penetration depths.

Chapter 5: In-Situ OCT Measurement of Single Scan Lines

5.1 Introduction

After having developed the integrated OCT/SLS system, the focus moved to the third objective of this work, namely, to use the OCT/SLS machine to detect defects common to SLS. As far as where to start imaging with OCT in the SLS machine, it made sense to start with individual scanlines since individual scanlines are the building blocks of all SLS builds. This work is revised and expanded from previously published work [23].[4]

5.2 Methods

For this study, a powder bed of virgin nylon powder was spread, the LAMPS machine was heated to temperature, and various lasing and imaging of individual scanlines was performed. To examine the utility of OCT in detecting sub-surface changes, an experimental protocol was developed in which the CO_2 beam first sintered two reference points 4 cm apart on a nylon powder bed (2.5 W laser power for 0.1 seconds each). When the experiment was designed and carried out, neither the synchronization of the OCT and position data nor the automatic sectioning algorithm had been developed. Therefore, the marking holes were necessary to identify the OCT beam location in the resultant OCT data,

[4] This chapter contains work previously published in A. Lewis, M. Gardner, A. McElroy, T. Milner, S. Fish, J. Beaman, In-Situ Process Monitoring and Ex-Situ Part Quality Assessment of Selective Laser Sintering Using Optical Coherence Tomography, in: Process Development, Austin, TX, 2016. In that work, the primary experimental design, imaging, and analysis presented was performed by A. Lewis.

and were used to manually register the images. After these holes were formed, the CO2 beam sintered a 2.5 cm line directly between the two marking holes. This line was sintered in repeating experiments with various laser powers (20%, 40%, 60%, 80% and 100%). For each experiment, the OCT system captured a series of A-scans at 100 kHz during each of these sintering steps and continued to collect B-scan images of the sintered area for approximately 3 seconds after the nylon was sintered in order to monitor surface and sub-surface variation as shown in Figure 32.

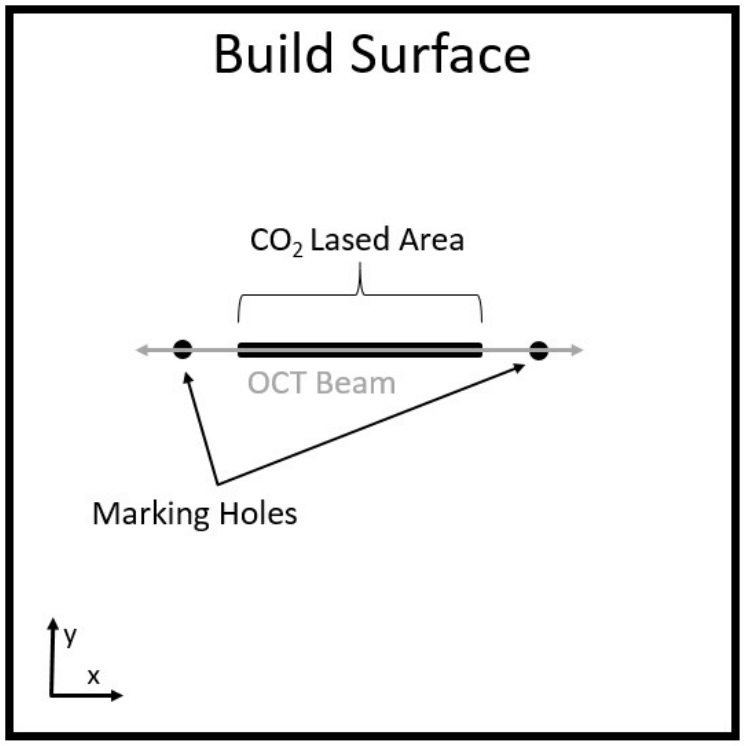

Figure 32: Schematic of the Single Layer Scan Line Test is shown. The dark gray represents areas of sintering of nylon while the light gray represents the imaging path.

5.3 Results And Discussion

As mentioned earlier this test was run several times at different CO_2 laser powers. Images from this test using the highest laser power of 32.5 W are shown in Figure 33 after applying a non-local means de-noising filter [36–38].

The top image of Figure 33 is a pre-lase scan. The marking holes are indicated as well as several other features. The concurrent image/lase scan appeared nearly identical to the pre-lase scan and is not shown here. The middle image is the post lase scan taken about 0.1 seconds after lasing shows the melted region developing. The bottom image is the post lase scan taken about 0.5 seconds after lasing.

The lased region didn't develop much further after this point until the end of the 3.2 second data collection period. In the bottom image, the melted scan line is easily visible. It is characterized by a reflecting top surface, followed by a transparent, homogenous liquid region with the unsintered powder strongly scattering below the liquid region. Additionally, it can be seen that the melted region is deeper on the right side of the image at the beginning of the scan line (scanline was scanned right to left).

This observation agreed with images from other builds taken with a bore-sighted long wave infrared camera (LWIR) as shown in Figure 34. The hot spot and resulting deeper meltpool was caused by the laser galvonometers accelerating at the beginning of each scan line and thus depositing more power at the beginning of each scan line. The additional power results in a deeper region being melted at the beginning of the scan line in this test.

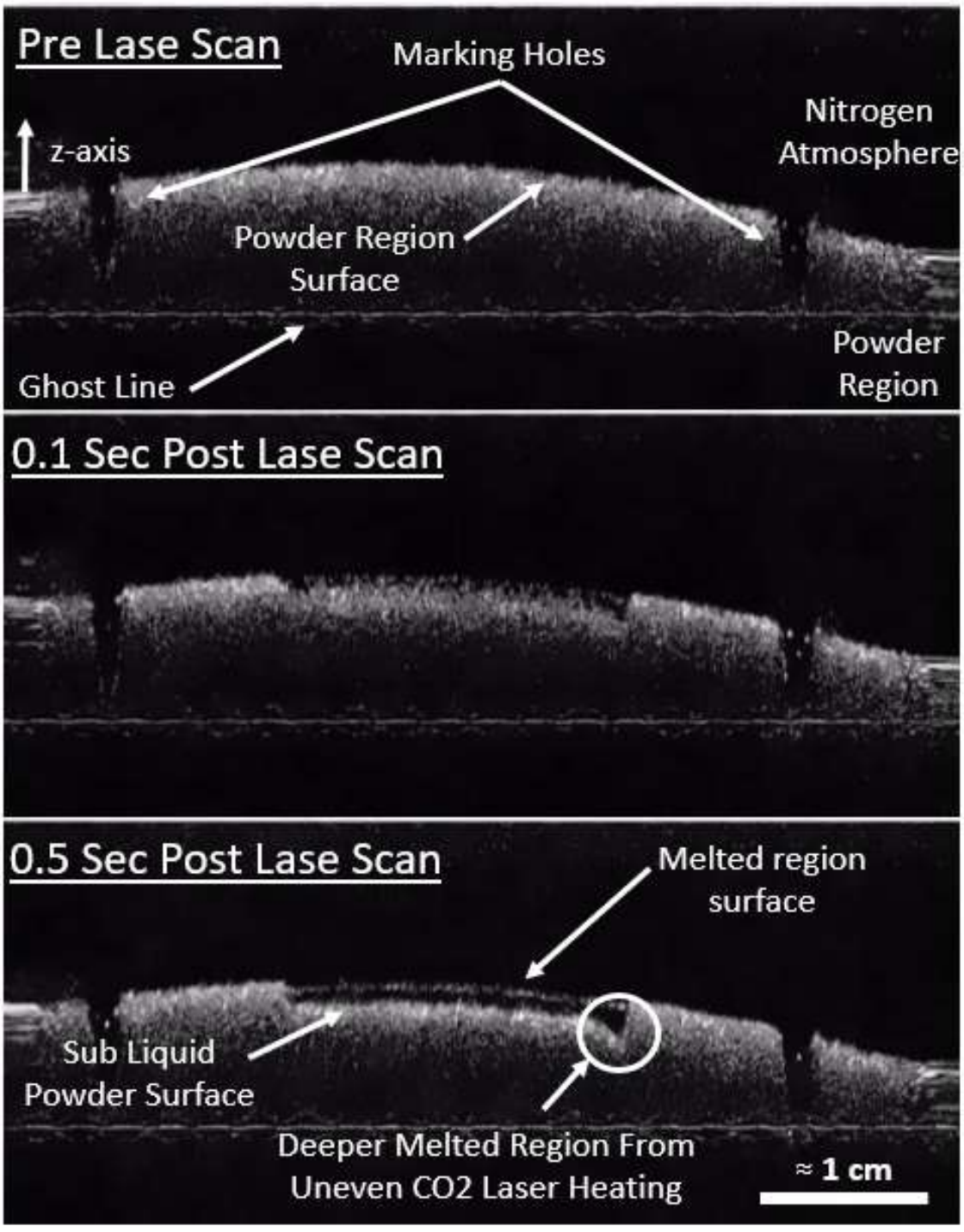

Figure 33: (Top) Pre-lase Scan (Middle) Post Laser Scan Taken about 0.1 seconds after lasing (Bottom) Post Lase Scan taken about 0.5 seconds after lasing.

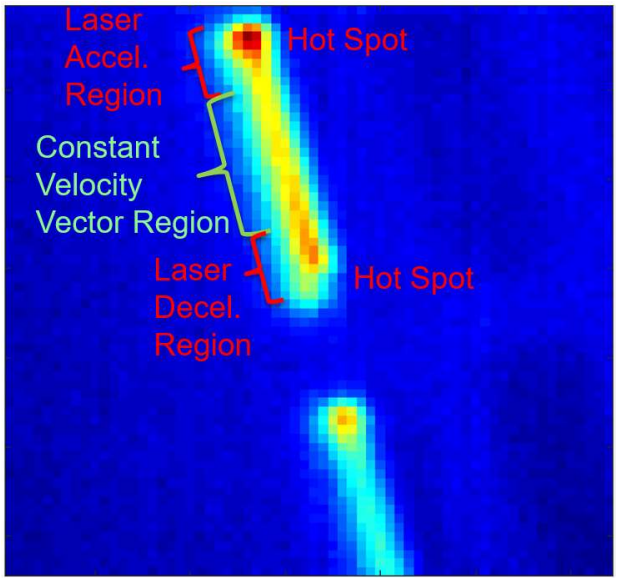

Figure 34: Thermal image taken of a few scanlines in an SLS build with a LWIR camera

Figure 33 shows only the results from the highest laser power used which is significantly higher than the 12 W laser power typically used in nylon builds in the LAMPS machine. The same features mentioned above were present in the lower laser powers, though less pronounced. Additionally, with the build surface temperatures set lower than those used for a typical build, the additional laser power provided the extra power needed to fully melt the scanned portion.

In order to quantitatively report on the results from the different laser powers additional image processing was performed including 2nd order interleaving and curvature correction as described in Chapter 4 as well as applying a block matching three-dimensional (BM3D) filter [39]. The bottom surface of the melt pool was found by a

second edge detection algorithm. Finally, the meltpool depth was calculated as the mean distance from the top surface, and the excessive heat error was recorded as the max distance of the meltpool edge from the meltpool mean depth. This process is illustrated in Figure 35 below.

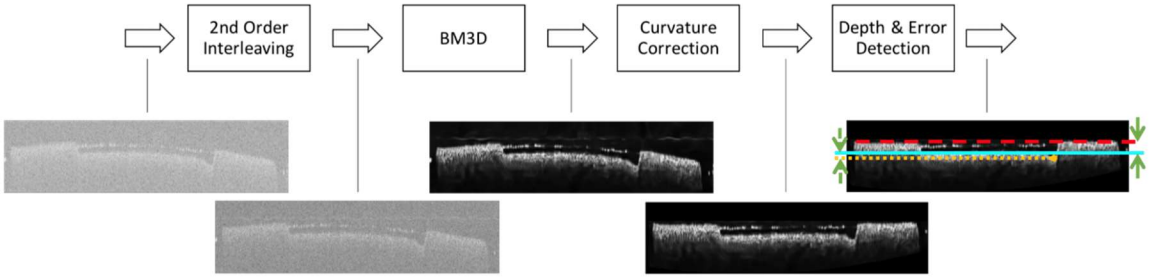

Figure 35 To obtain the final image and metrics for analysis, a series of image processing steps are performed, including second-order interleaving, BMD3 filter, curvature correction and depth/error detection.

The results of the processing are shown in Figure 36. The OCT images reveal the top surface of the nylon powder and the top and bottom surface of the meltpool. The OCT images also showed sub-surface flaws in the build due to excessive heating. As the laser power increased from 20% (4.6W) to 100% (32.5 W), the average meltpool depth increased monotonically from 0.01 mm to 0.17 mm. Likewise, the excessive heat error also increased as a function of laser power from an average of 0.02 mm to 0.12 mm.

It was anticipated that greater sintering laser powers would yield a deeper meltpool because of a larger temperature gradient. However, the OCT system detection of the hot spot and deeper meltpool illustrates the utility of a three-dimensional imaging approach and OCT in particular as the actual depth information could be detected which would not

be possible with conventional imaging sensors. Given this information, laser power could be responsively varied to minimize the excessive heat error in an offline manner, and perhaps even with real time control with the use of hardware such as a Field Programmable Gate Array (FPGA).

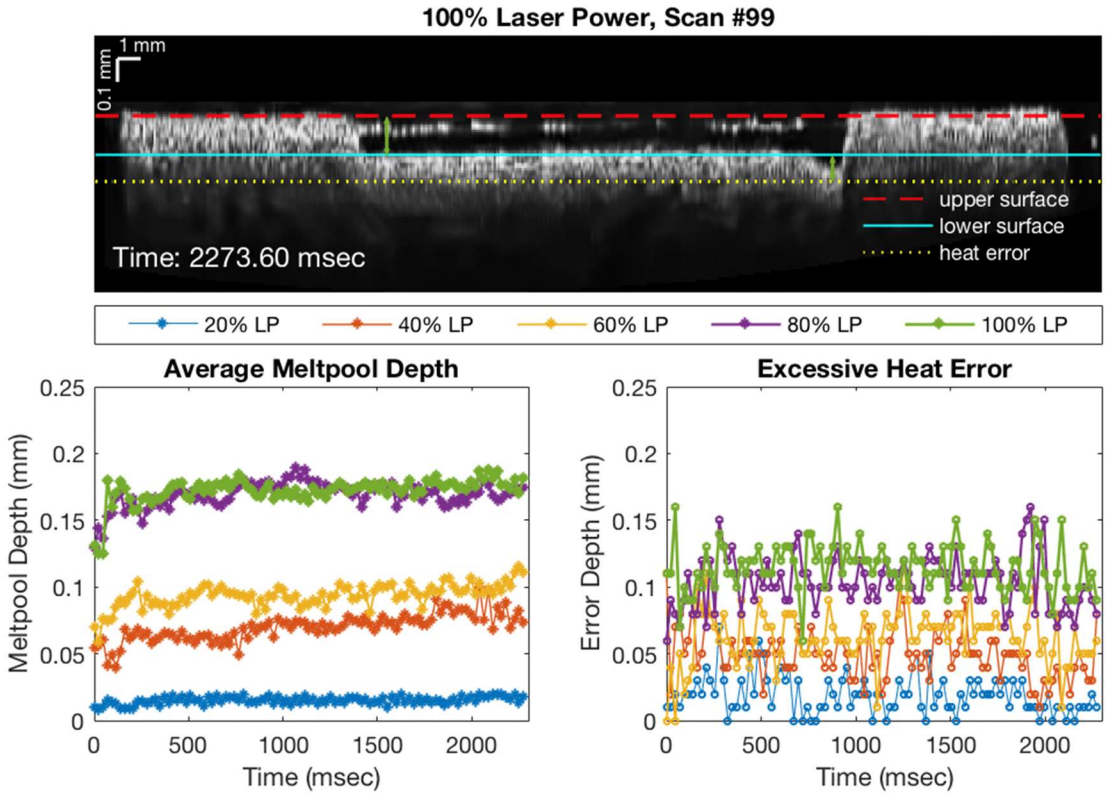

Figure 36 OCT imaging after sintering reveals a slight upward trend in average meltpool depth with time as the heat diffuses through the powder bed. Also, increasing laser powers create deeper meltpools and larger excessive heat errors on the temporally distal end of the sintering laser sweep (right side).

As expected, false curvature limited the build area for OCT imaging as detailed in Figure 37. In this case, due to the OCT system's imaging depth, any surface that had a pathlength difference of greater than 3.7 mm was aliased in the OCT fringe as a lower-

frequency component and thus unreliable for interpretation. With the field curvature induced by post-objective scanning and the OCT system's imaging depth, the build area is limited to a circle with a 64 mm radius, where the center point appears as the shortest pathlength difference (Distance 0,0 in Fig. 6), and the edges are the longest pathlength difference. Down- sampling for second order interleaving further limited the field of view to a circle with 45 mm radius. The possible imaging area is shown within the circles in the en-face depiction of the build surface shown in Figure 37 below.

5.4 CONCLUSIONS

In this chapter, individual scanlines were studied by OCT imaging them as they cooled directly after lasing them. It was observed that at least one defect could be observed with OCT. The defect was over heating due to laser galvo acceleration. The results confirmed what had been seen with high speed LWIR cameras, but the increased melt depth was able to be quantified from OCT data unlike from thermal camera data. Additionally, the overheating defect was found to be repeatable at various laser powers and the melt pool depth was quantified for each of five different laser powers. Finally, speculation was made on how OCT data and the detection scheme presented here might be used to reduce the overheating defect.

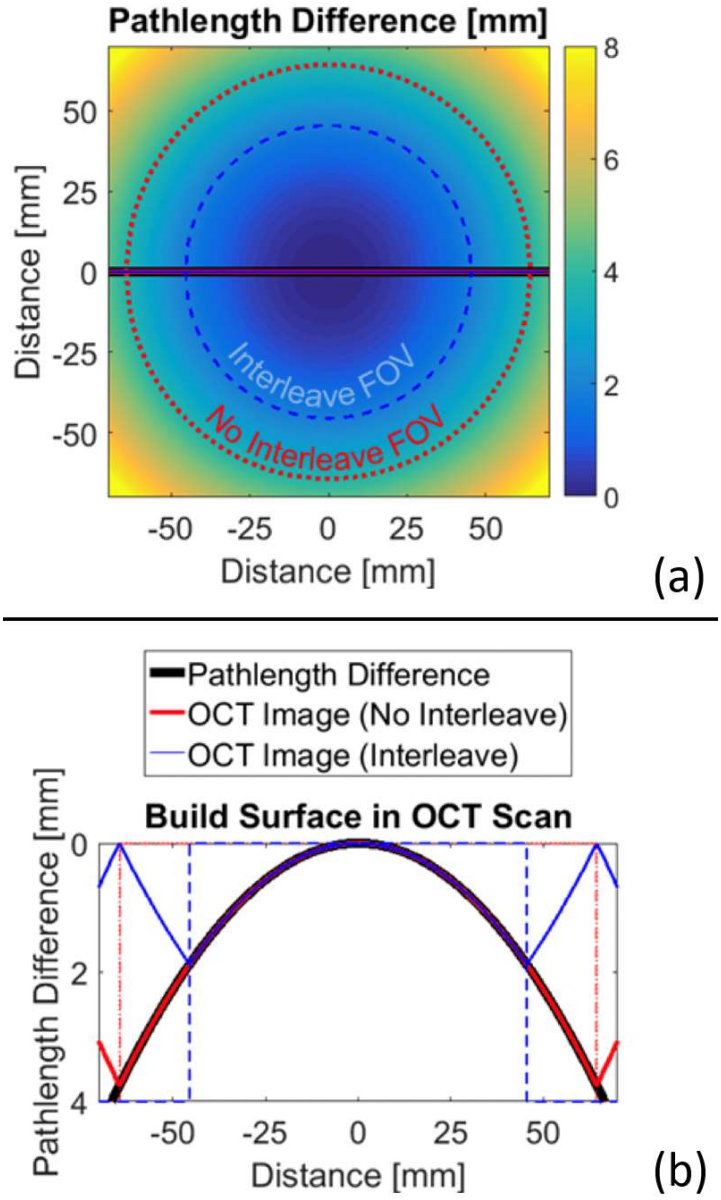

Figure 37: The imaging range of the OCT system limits the field of view (FOV) because post-objective scanning hyperbolically varies the pathlength difference between the flat powder surface and the static reference arm mirror. The FOV and cross-sectional image with no interleaving is pictured by the red lines. The FOV is smaller after interleaving (blue), and the corresponding cross-sectional image exhibits faster aliasing due to downsampling in the k-space domain.

Chapter 6: In-situ Curl Detection using Optical Coherence Tomography

6.1 Introduction

As mentioned, the objective of these final chapters in this work is to use the OCT sensor to detect flaws in the SLS process in-situ. After having detected melt pool depth and overheating at the end of a scanline in the previous chapter, the focus was changed to detection of surface curl. In the SLS process, if the powder bed temperature is too low, thermal gradients will cause the edges of the sintered area to curl upwards. This curled region is problematic when manufacturing parts with SLS because if the curl is severe enough, the raised region of the part will catch on and be dragged by the powder spreading element as it travels across the powder bed. This prevents subsequent layers from being sintered in the correct positions relative to the dragged, previously sintered layers [16]. As a surface feature, detection of surface curl has a high probability of being detected with OCT. This study confirms the ability of OCT to quantitatively measure the extent of surface curl in the Selective Laser Sintering process. This work is revised and expanded from work published previously in conference proceedings [40].[5]

[5] This chapter contains work previously published in A. Lewis, S. Fish, J. Beaman, Capabilities and Limitations of Optical Coherence Tomography as an In-Situ Sensor for Curl and Porosity Detection in Selective Laser Sintering of Nylon 12, in: New Developments in Measurement Techniques, Sheffield, United Kingdom, 2019. In that work, A. Lewis performed the primary experimental design, data collection, and analysis presented.

6.2 METHODS

For this experiment, the powder bed was heated to a temperature on the lower end of the acceptable range of build temperatures in order to be sure to induce surface curl in 3 long thin bars shown in Figure 38(a). On the first and last 15 layers and approximately once every 10 layers during the middle of the build, the build surface was imaged with OCT in the area where the parts were being built immediately after being lased with the sintering laser. For this build, the powder bed set temperature was 178ºC. The laser power at the powder bed surface was 8.8W, with a spot size of 575 μm. The scan speed was 1500 mm/s, and the hatch spacing was 212 μm. The scan lines alternated between +45º and -45º angle each layer. Figure 38(a) shows the geometry of the part which is 165 mm long, 8 mm wide not including the tabs, and 10 mm tall. Figure 38(a) is oriented differently from the rest of Figure 38 in order to better show the geometry of the parts.

The XCT data was collected using a North Star Imaging upgraded version of an ACTIS scanner using 120kV, 0.15 mA and 3600 projections. The data was reconstructed into 16 bit TIFF images producing data divided into cubic voxels with each side being 16.3 μm in length. Subsequent image processing and analysis was performed using FIJI, a distribution of ImageJ [29,30].

6.3 RESULTS AND DISCUSSION

After performing the curvature correction described in Chapter 4 on the OCT data, curl was easily identified visually on the left side of the part. Figure 38(b) is the en face OCT image of the build surface on layer 10 and shows the three specimen being built. The

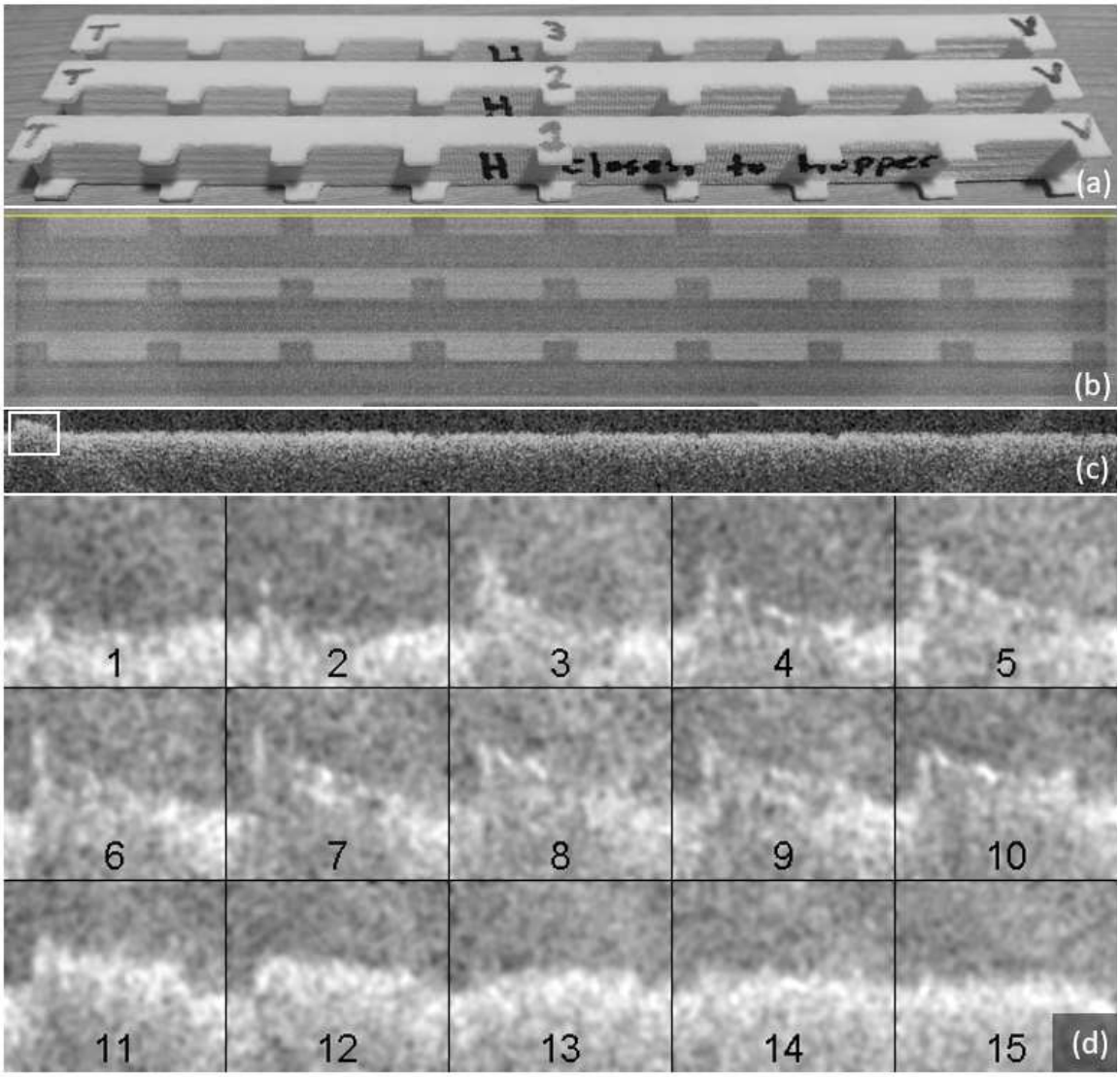

Figure 38: (a) printed parts visual image (b) an en face image of layer 11, (c) a b-scan just above the top part as indicated by the solid line in (b), (d) a montage of the area in the white rectangle of (c) from every dataset for layers 1-15.

b-scan located just above the top specimen as indicated by the yellow line is shown in Figure 38(c). Figure 38(c) shows a flat powder surface with a noticeable raised section on the left of the image. This raised portion is surface curl. The area corresponding to the white rectangle is shown for each of the first 15 layers of the build in Figure 38(d). The

curl started on the left side of the first layer. The maximum height of the curl grew on each of the first 7 layers after which it began to decrease.

The following algorithm was used to detect the height of each A-scan in the image. First, the 3D dataset was opened. The average A-scan intensity was calculated then subtracted from each A-scan in the dataset in an attempt to reduce noise present in the OCT images. A Gaussian blur filter with a radius of 3 pixels was then used to further smooth the effects of noise. The curvature of each dataset was then corrected as described in Chapter 4. A region of interest (ROI) was selected at the top of the dataset above the powder surface and curl and the noise threshold was determined to be the maximum pixel value in the ROI region in the dataset. The surface of each A-scan was determined to be the first pixel with an intensity above the noise threshold. Any A-scan without a pixel above the noise threshold was set to a null value and not used in further calculations. The height values were then plotted vs. their x-y position. One such height map of layer 10 is shown in Figure 39(a) below. The range of the color scale has been set to emphasize raised areas in white. Figure 39(b) is a montage of the leftmost portion of each height map from layers 1-15. Figure 39(c) is a plot of the average height of the curled subregions from Figure 38(d).

It was also possible to plot the height of each area of the entire powder surface on a false color scale. The resulting image looks similar to the en face image, but the useful difference is that the pixel intensity values correspond with the actual height of that region of the build surface. Such a figure is shown in Figure 39(a) and (b).

The curl around the top and left edges of the specimen can be clearly seen in Figure 39(a) as regions brighter than neighbouring pixels. Figure 39(b) shows how the curl

progresses at each area shown on each layer. The tabs along the top of each specimen are 10 layers thick. Figure 39(b) shows that despite not sintering the powder together in the tab region on layer 11, the powder area in the tab region was still higher than the surrounding areas. This suggests that the cold powder causes curl which is then reduced when the laser melts the powder together and removes voids in the powder. Data such as this suggests raising the set temperature of the heaters which heat the feed powder before it is spread

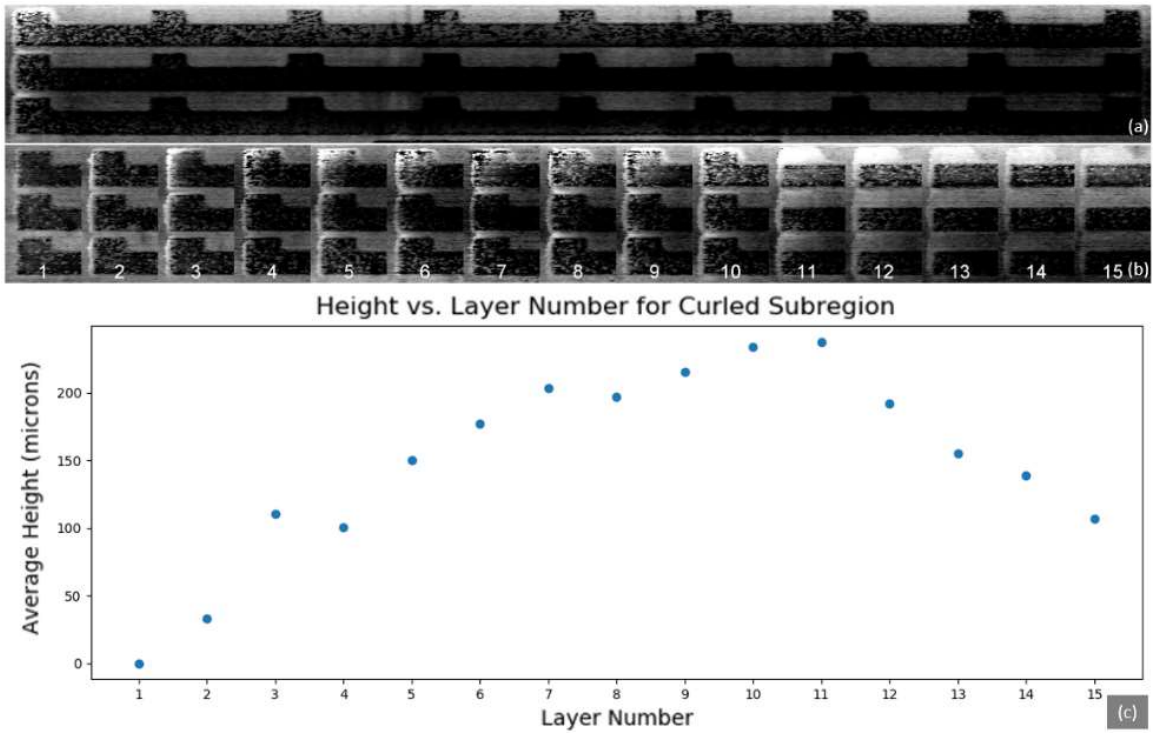

Figure 39: (a) en face image from layer 10 of the build (b) part of the en face image for layers 1-15 (c) plot of average height of the curled subregion vs. layer number

may reduce curl. Figure 39(c) is a plot of the average relative height vs the layer number for the curled sub region shown in Figure 38(d). The data tracked the increasing curl over

the first 11 layers and its decrease thereafter. A common problem in SLS is that curl becomes sufficiently high that the curled part contacts and is dragged by the roller as it spreads new powder, usually resulting in a failed build. Automated generation of data similar to that shown in Figure 39 could be used to warn of a build that is likely to fail soon.

6.4 LIMITATIONS

Quantification of curl in SLS is limited by the axial and lateral resolution of the OCT system being used, about 7.9 and 186 μm respectively. Additionally, using the height detection algorithm mentioned above, the surface was not able to be calculated at every point on the build surface. Scanning for height also extends the build time for each layer by a few seconds since the height scanning is done separately from the sintering scan. One strategy to reduce the imaging time necessary might be to only image areas likely to be problematic for curl such as the outline of the parts being built.

6.5 CONCLUSIONS

In this study, SLS curl bars were built. The build temperature was colder than usual in order to induce surface curl in the part. A height detection algorithm was presented, and an en-face view of the data was shown with height in false color. Curl was tracked and insight was gained on when curl occurs. Suggestions are given on how automated detection might be implemented and how it might be useful in SLS builds. Additionally, limitations of the detection of curl in SLS were also described.

Chapter 7: In-situ Porosity Detection with Optical Coherence Tomography

7.1 Introduction

Improving quality validation is consistently identified as a critical area of improvement for SLS in industry roadmaps [17,18]. One common defect known to decrease the strength of SLS parts is porosity. Porosity within a part decreases the effective cross-section, and in turn decreases the strength of the part. This has been demonstrated by several researchers in SLS parts specifically [10,11,41]. The ability to detect porosity during a build is an important step towards qualifying the integrity of SLS parts during fabrication as well as researching strategies to reduce or eliminate pores and thereby improve strength. OCT images are formed as light reflects off of material or phase interfaces in a sample. Pores within a melted nylon region in an SLS part during the build are such an interface, and given a high enough signal, should show up in OCT images. In this study, Optical Coherence Tomography is used to image a selective laser sintering part during a build. After being built, the part is imaged with X-ray Computed Tomography (CT). The comparison between the OCT and XCT images makes clear that at some part porosity is visible in the OCT images.[6]

[6] This chapter contains work previously published in A. Lewis, S. Fish, J. Beaman, Capabilities and Limitations of Optical Coherence Tomography as an In-Situ Sensor for Curl and Porosity Detection in Selective Laser Sintering of Nylon 12, in: New Developments in Measurement Techniques, Sheffield, United Kingdom, 2019. In that work, A. Lewis performed the primary experimental design, data collection, and analysis presented.

7.2 METHODS

For this experiment, the powder bed was heated to a temperature of 192°C. A cylinder 30 mm in diameter, and 3 mm in height was built. Several geometric markers were designed on the bottom of the cylinder to facilitate alignment between the OCT and XCT data. The part consists of 5 orientation marking layers and 30 main cylinder layers. The part was imaged with OCT once every 10 layers during the build. The laser power at the powder bed surface was 12.8W, with a spot size of approximately 650μm. The scan speed was 1500mm/s, and the hatch spacing was 279μm. The scan lines alternated between 0° and 90° angle from the x-axis on each layer, and each layer included an outline scan. An image of the part geometry generated with CAD software is shown in Figure 40 below. The cylinder was imaged with OCT during the build after each layer was sintered. It was not necessary to correct for the false curvature explained in Chapter 4 because the cylinder was built very close to the center of the build surface resulting in minimal curvature distortion. The follow up build parameters were similar to the firs build, except the cylinder built had only 20 main layers instead of 30.

The XCT data was collected using a North Star Imaging upgraded version of an ACTIS scanner using 120kV, 0.15 mA and 3600 projections. The data was reconstructed into 16 bit TIFF images producing data divided into cubic voxels with each side being 16.3 μm in length. After imaging the data with XCT, the data sets were aligned using the orientation markings. The alignment step and subsequent image processing and analysis were performed using FIJI, a distribution of ImageJ [29,30].

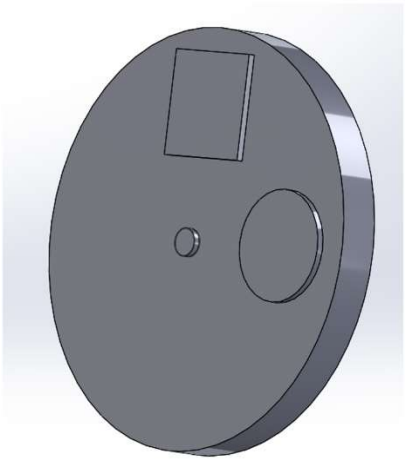

Figure 40: Cylindrical Specimen for Porosity Experiment

7.3 RESULTS AND DISCUSSION

7.3.1 Initial Build

Figure 41(a) shows a B-scan from the OCT data taken after the final cylinder layer was sintered. Figure 41(b) shows an en face image from the same dataset. The solid lines on the B-scan indicate which depths of the image were used to generate the en face image. The solid line on the en face image indicates which B-scan is being shown in Figure 41(a). The sintered cylinder region is much more transparent in the top several layers than in the surface curl data set in Chapter 6. This is due to the higher build temperature and/or laser power used in this build versus the surface curl build. A highly scattering layer appears beneath the surface as indicated in Figure 41(a). Based on the depth from the surface, the highly scattering layer is approximately layer 23 of 30 in the build.

The highly scattering layer 23 seen here did not extend across the whole cylinder, but was limited to the upper portion of the cylinder as indicated by the bright area of the cylinder in Figure 41(b). Additionally, there are various, small segments of layer 23 which are shadowed by something above it. Figure 41(c) shows a contrast-enhanced, magnified view of the area within the dashed lines from 6(a). In this enhanced image, two bright spots appear above the shadow. This is consistent with a pore which would scatter light at the top and bottom surfaces, and could leave too little focused light to image beneath the pore. This pattern of a shadow beneath two bright spots was seen in many instances in this dataset, though shadows without discernible scatterers above them were also present. This could be explained by insufficient OCT signal being collected to detect some pores in the part. Another notable feature in Figure 41(a) is the upward curved portion of layer 23. The XCT data shown in Figure 41(d) depicting approximately layer 20 of the cylinder shows a large pore approximately 0.9 mm in diameter in the same area as the curvature. It is possible that a bubble formed on the surface of the part there, and remained even as powder was spread on top. This may have caused the curvature seen in Figure 41(a) and 6(c) though this data alone is not conclusive.

Figure 42(a) shows a cropped, close up of the en face image in Figure 41(b). The data at the depth of the highly scattering layer 23 is used to generate this en-face image. The highly scattering layer was only present on the upper portion of the cylinder so only the upper portion is shown in Figure 42(a). Figure 42(b) shows a cross-section from the XCT data showing approximately layer 28 of the cylinder.

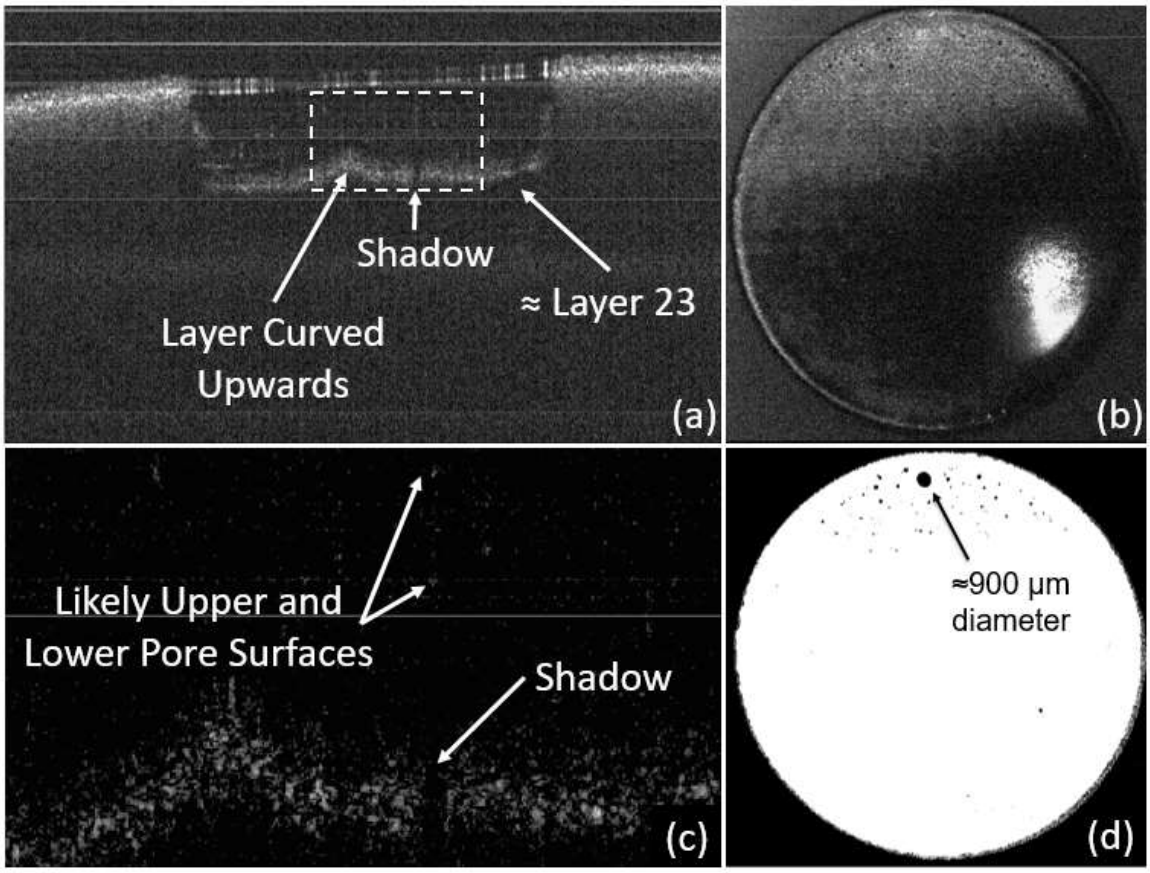

Figure 41: (a)-(c) are OCT images generated from the dataset captured after the last cylinder layer was sintered. (a) A B-scan with several features indicated (b) the en-face image (c) a contrast enhanced, magnified image of (a) is shown (d) XCT cross-section showing ≈layer 20

There is good agreement between the OCT and XCT data for the larger pores. The en-face OCT image is somewhat noisy, and a standardized pore detection algorithm has not yet been used. Further work is required to detect and calculate the proportion of the large pores which were able to be identified with OCT. Some of the smaller pores seen in the XCT are not visible in the OCT en face image likely due to being smaller than the

resolution limit of the OCT system used in these experiments which was approximately 186 µm. For scale, the pore circled in blue in Figure 42 has a diameter of about 260 µm.

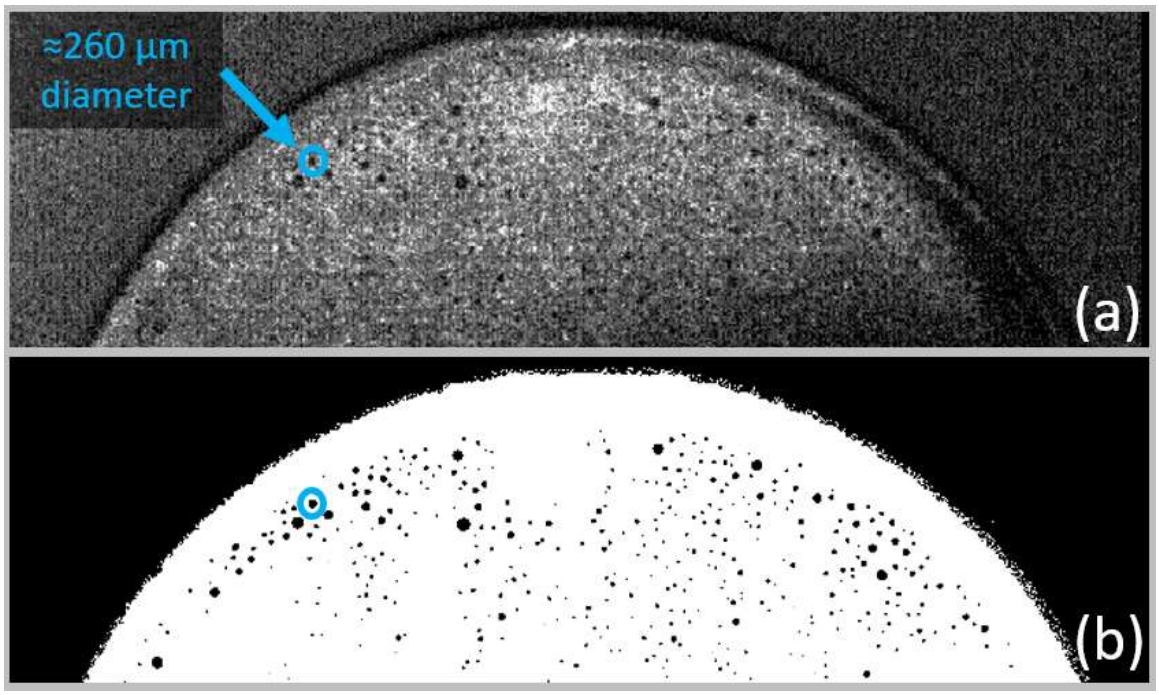

Figure 42: (a) en face image of the cylinder generated from the highly scattering layer depths of the OCT data (b) XCT cross-section of approximately layer 28 of the 30 cylindrical build layer

7.3.2 Follow-Up Build

The initial porosity detection build confirmed that some pores were visible with the OCT imaging data, but questions still remained. Were the curved regions in Figure 41(a) and (c) caused by a bubble forming as suspected? If so, are the bubbles detectable with OCT as they are formed? To answer these questions a follow-up build was performed as explained in Section 7.2.2. Select data is shown in Figure 43. Figure 43(a), (b), and (f) show a b-scan and an en-face OCT image for layers 1, 2, and 3 respectively. Figure 43 (c),

(d), and (e) show corresponding thermal camera, XCT, and OCT data. Figure 43 (g) shows thermal camera image from layer 3. In layer 1, as shown in Figure 43(a) the surface appears flat except for a slight curvature due to the field curvature of the OCT system as described in Chapter 4. In Figure 43(b), layer 2 shows a bubble has formed which is evident by the sharply protruding surface. The bubble is seen in the b-scan as well as the en-face image.

In the b-scan, the bubble is noted by a brightly reflecting flat region at the top and bottom bubble surfaces, as well as a lack of brightness on the bubble surface with greater curvature. Figure 43(c) shows the bubble is also visible on the infrared camera, and Figure 43(d) confirms the bubble is evident in the XCT data as well. Figure 43(e) shows the OCT en-face image from layer 2 again for comparison with the thermal and XCT data. Figure 43(f) shows OCT data for layer 3 and shows the bubble is still protruding above the surface, but less so than before since a fresh layer of powder has been spread and sintered together around it. The bubble is still apparent in the en-face image as well. Figure 43(g) shows that the reduced bubble is no longer visible on the thermal camera data.

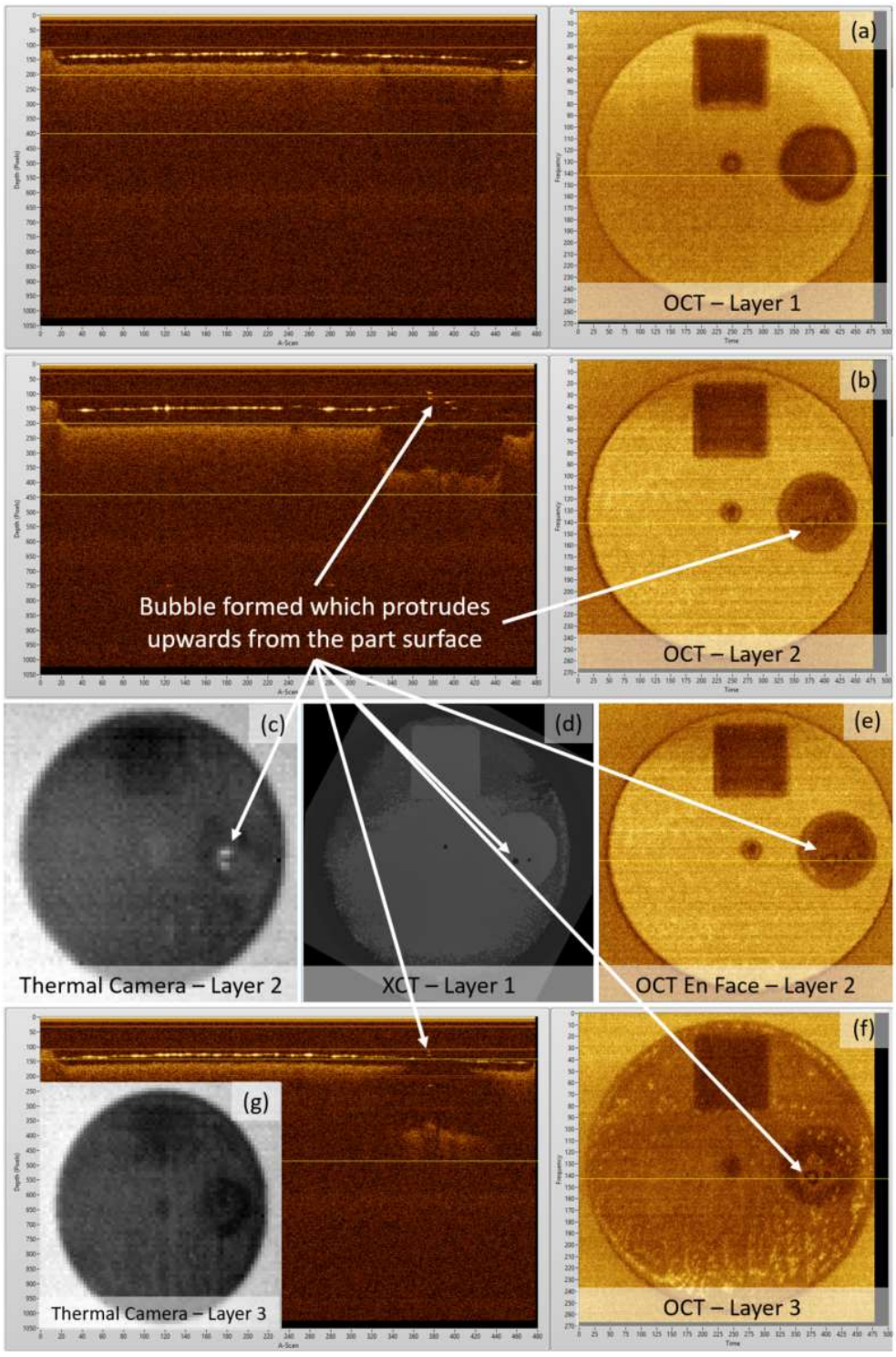

Figure 43: OCT, XCT, and Thermal Camera data show a surface bubble as labeled

Figure 44 shows data from the next several layers of the build. Figure 44(a), (e), and (g) show an OCT b-scan and en-face image for layers 4, 5, and 20 respectively. Figure 44 (b), (c), and (d) show corresponding thermal camera data, XCT data, and OCT en-face images for layer 4. Figure 44(f) shows thermal camera data for layer 5. After layer 4 was sintered, many more bubbles formed. Figure 44(a) shows the top and bottom surfaces of the largest new bubble as well as the bubble viewed earlier in Figure 4. The brightly scattering top and bottom surfaces are indicated. Figure 5(b) shows that 3 of the new bubbles again were visible on the infrared camera. Figure 5(c) and (d) show that there is good agreement between the XCT and OCT en-face image as to pore location. It should be noted that the circle in the center of Figure 5(d) though it appears similar to a pore, it is actually the orientation geometry, and not a pore, and thus does not show up as a pore in the XCT data in Figure 5(c). Figure 5(e) shows OCT data for layer 5. Again, the pores are visible, but additionally, it can be seen that the powder beneath the surface of the pore appears raised as indicated. This is consistent with a pore because OCT imaging is based on time of flight of the light. As the OCT laser travelled a greater distance through the gaseous pore which has a lower index of refraction, the image beneath the pore appears shifted up relative to the rest of the image. Finally, Figure 5(g) shows the OCT data at the end of the build. The en-face image for layer 20 appears similar to the en-face image for layer 5 because no more bubbles appeared over the course of the short 20 layer build though it is not clear why not. In Figure 5(g) the top and bottom surface of one of the pores was still visible and is indicated. The top and bottom surface of the pore on the right hand side of the frame is no longer visible, perhaps due to attenuation of the signal through the melted nylon.

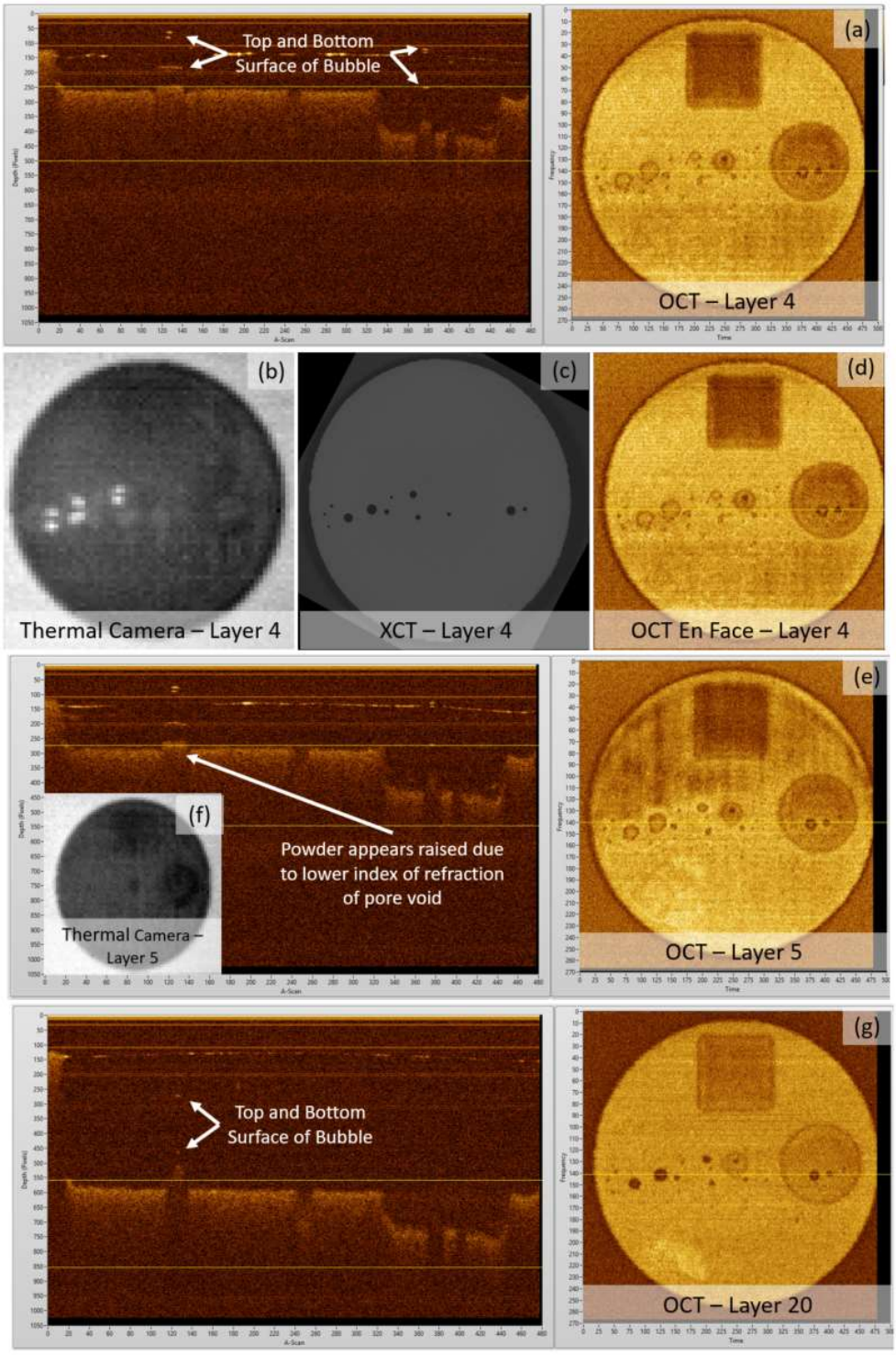

Figure 44: Additional OCT, XCT, and Thermal images of surface bubbles as labeled

7.4 CONCLUSIONS

The builds in this chapter were performed at higher powder bed set temperatures than the build done in Chapter 6. This caused increased homogeneity of the liquid part during the build. This in turn made possible the viewing of part porosity with the OCT data taken during the build since most layers in the resulting OCT images were much more transparent than those in Chapter 6. In the first build an occasional highly scattering layer was present in the part which prevented imaging below that layer. Pores were shown to cast shadows beneath them, and by generating the en face image based on the data at the highly scattering layers, the pore x and y locations could be identified. The z location of the pores was indicated for some pores by scattering at the pore top and bottom interfaces. Comparison of the pore shadows was done with pore locations from the XCT data, and good agreement was seen for larger pores on one layer. Additional work would be required to characterize what percentage of pores of what sizes agreed with the XCT data. In the first build, a few pores that were much larger than all the other pores were noted. This caused the authors' to hypothesize that a different mode was responsible for creating these pores. A second build was performed to investigate this more fully. Through imaging on every layer, it was apparent that at high build temperatures and laser powers, bubbles form on the surface of the part which are then covered with powder and result in a large pore, many times larger than other pores within the part.

Chapter 8: Conclusions and Future Work

8.1 Summary of Contributions

The contributions of this work add to the expanding body of research related to improved sensing and control of the selective laser sintering (SLS) process. Chapter 2 discusses the feasibility of flaw detection using an Optical Coherence Tomography (OCT) sensor by imaging SLS Nylon 12 powder in the virgin powder, melted, and resolidified forms with an OCT sensor on the benchtop. It was shown that OCT was able to image through liquid nylon 12 and resolidified nylon 12 to a lesser extent. This showed promise for in-situ SLS defect detection with OCT sensors.

Chapter 3 sought to improve understanding and OCT imaging depth in SLS nylon 12 parts and powder. First, the cause of the limited OCT imaging depth in nylon 12 powder was investigated, and intra-particle and inter-particle multiple-scattering were shown to be the cause. The OCT imaging depth was improved in nylon 12 parts and powder with the use of ethyl cinnamate as the imaging media. Finally, nylon spherulites were shown to be a strong source of scattering in the resolidified nylon 12 part by continuously OCT imaging a nylon 12 powder sample through the melting and resolidification/recrystallization process.

The integrated OCT/SLS system including data processing software & hardware were detailed in Chapter 4. First, the optical design was presented and characterized. Afterwards, process of registering the of OCT data with position data was explained.

Finally, methods for curvature correction, background signal subtraction, and data interleaving was discussed as methods to improve imaging artifacts and reduce noise.

In Chapter 5, the integrated OCT/SLS system was used to examine individual scan lines. Uneven melting depth was detected due to laser galvo acceleration. Scanlines were recorded through the melting process for various laser powers. The melt depth was able to be quantified for each of five different laser powers, each exhibiting the uneven melt depth defect.

Chapter 6 and 7 study OCT's ability to detect various typical defects in SLS builds. Chapter 6 studied OCT's ability to detect surface curl in SLS parts. A height detection algorithm was presented and an en-face view of the curl data was shown in false color. Recommendations for automated detection during the SLS build process are given as well as limitations of curl detection. In Chapter 7, porosity was detected with an OCT sensor during the SLS build process at high build temperatures. Pores were shown to cast shadows beneath them, and by generating the en face image based on the data at the highly scattering layers, the pore locations were shown to agree with the locations of pores in the XCT data. Additionally, some large pores were found to be caused by the formation of bubbles at the surface of the melted nylon. These pores were shown to be detectable on the same layer on which they were formed.

8.2 Future Work

The contributions this work adds to literature are very promising. For this reason, additional research focusing on improved data analysis and improved hardware/optical

configurations is recommended. The most promising areas of research, in the author's view, are presented below.

8.2.1 Automated Defect Detection

In the author's view, the most promising vein of research extending from the work presented here involves automation of defect detection using the OCT sensor and other sensor data. OCT has been shown to contain useful defect information in Chapters 5-7 including scanline overheating, surface curl, and porosity. Automating the detection process will be a step towards improved and more rapid SLS part qualification and further opens the way for experimentation with defect correction strategies. Traditional image processing could be used for automated detection, particularly in the case of surface curl, but machine learning methods should also be considered for automated detection of defects. One recently published paper by Gobert et al. in which in-situ visual camera information was used via machine learning for defect classification in metal powder bed fusion could serve as a good starting point for similar research. In their paper, they were able to identify pore defects with accuracy of around 80%, but the LAMPS machine has the advantage of being equipped with not only a visual camera, but also up to 2 infrared cameras, over 40 thermocouples, and the OCT system. This additional sensor data is likely to further improve the pore detection accuracy of a machine learning defect classifier.

8.2.2 Use of OCT sensor for real time feedback control of laser power

Another area of research that is promising is use of OCT as a sensor for real time feedback control of laser power in polymer SLS. Other research has shown real-time feedback monitoring for metal powder bed fusion additive manufacturing processes using a photodiode coaxial with the sintering laser beam with promising results [42]. This type of system would be difficult to implement usefully in a polymer SLS application due to the reduced signal to the photodiode stemming from the much lower temperatures of the process. However, OCT is a sensor that commonly has A-scan detection rates of greater than 50kHz. Individual OCT A-scan data could likely be analyzed with an FPGA for a similar type of real-time monitoring and/or control in powder bed processes. As yet, it is unclear how useful individual A-scans will be in predicting defects in parts. This would need to be established as well in order to determine the control scheme based on A-scan data. Machine learning may be valuable in this aspect as well.

8.2.3 Use of Polarization Sensitive OCT for Improved Imaging

The current OCT system does not differentiate the backscattered radiation by polarization. The spherulitic crystals in the nylon powder is known to be highly birefringent while the homogeneous, nylon melt is presumably less so due to the absence of crystals. Therefore, it is likely that OCT will be useful in detecting melting and resolidification rates during the SLS build process. The same information that is currently obtained with the OCT system would still be available for other uses, and the polarization

differentiation may improve the results of the research studies listed in this work and in Sections 8.2.1 and 8.2.2.

8.2.4 Additional Improvements to the OCT Sensor for SLS applications

The suggestions listed below would improve the capabilities of the OCT set up on the LAMPS machine and would generally be useful in other SLS machines trying to [43] integrate OCT themselves. Implementation of the following suggestions is not ground breaking in itself, they would however improve the capability of the SLS/OCT system for other research purposes.

First, improvement of the lateral resolution in the OCT system would be useful for pore detection. The lateral resolution of the current system was simulated to be 186 microns. Although many pores in nylon SLS parts are larger than that size, many are smaller as well. Lateral resolution could be improved in one or both of the following ways. First, deconvolution could be used to improve resolution. The data collected in the experiments in this work was oversampled by a factor of 6. Deconvolution of OCT images in systems with large focal lengths has been studied and the application of such work to the LAMPS OCT system could improve resolution improving detection of smaller pores [43]. Computational cost of deconvolution of the data could limit the applicability of this method.

The second method to improve of the lateral resolution in the OCT system is accomplished with optical hardware upgrades. The lateral resolution is limited by the diffraction limited spot size of the laser used in the OCT system as described in Equation

4 where Δx is the diffraction limited spot size, λ is the wavelength of the laser, M^2 is the beam mode parameter, f is the lens focal length, and D is the input beam diameter at the lens.

$$\Delta x = \frac{4\lambda M^2 \mathrm{f}}{\pi D} \tag{4}$$

Based on Equation 4, the OCT system lateral resolution could be improved choosing a laser with a smaller central wavelength, decreasing the lens focal length or increasing the beam diameter at the lens. Changing the central wavelength is one option, though the optical studies reported in this work were all performed using lasers with a central wavelength of 1310 nanometers. It is not clear if the optical property insights reported will still hold at a reduced wavelength. Decreasing the lens focal length is difficult as well since the lens should be kept outside of the build chamber in order to remain within operating temperatures and remain free of any powder within the machine which could damage the optic. The beam diameter is possible if a larger diameter collimator can be found, but may necessitate a large galvo mirror and window as well depending on the final diameter of the beam.

An additional improvement to the OCT system could be improvement of the imaging field of view with the use of a motorized delay line (MDL). Currently, the field of view of the OCT system is limited to about 50% of the build area of the LAMPS system. This is due to the larger imaging distance to the edges of the powder bed than to the center as described in Chapter 4. The increase in imaging distance is beyond the 8mm imaging length of the current OCT system. Imaging more of the build surface could be

accomplished with the use of a motorized delay line (MDL) in the reference arm of the OCT system. The motorized delay line is not likely to be fast enough to keep up with the laser galvos as it scans from the center to the edges of the powder bed. The MDL could, however, be actuated after the OCT system has scanned the interior of the powder bed. After actuation, the edges of the powder bed would enter the imaging range of the OCT system and could subsequently be imaged. This increase in the effective imaging are of the OCT system would allow more efficient usage of the space in the LAMPS machine. Increasing the amount of OCT data that could be captured on each layer of the SLS build.

Works Cited

[1] I. Gibson, D.W. Rosen, B. Stucker, Additive Manufacturing Technologies : Rapid Prototyping to Direct Digital Manufacturing, Springer, Boston, 2009.

[2] H. Zarringhalam, N. Hopkinson, N.F. Kamperman, J.J. de Vlieger, Effects of processing on microstructure and properties of SLS Nylon 12, Materials Science and Engineering: A. 435–436 (2006) 172–180. doi:10.1016/j.msea.2006.07.084.

[3] N. Hopkinson, C.E. Majewski, H. Zarringhalam, Quantifying the degree of particle melt in Selective Laser Sintering®, CIRP Annals - Manufacturing Technology. 58 (2009) 197–200. doi:10.1016/j.cirp.2009.03.001.

[4] C.E. Majewski, H. Zarringhalam, N. Hopkinson, Effects of Degree of Particle Melt and crystallinity in SLS Nylon-12 parts, in: Materials, Austin, TX, 2008.

[5] B. Van Hooreweder, D. Moens, R. Boonen, J.-P. Kruth, P. Sas, On the difference in material structure and fatigue properties of nylon specimens produced by injection molding and selective laser sintering, Polymer Testing. 32 (2013) 972–981. doi:10.1016/j.polymertesting.2013.04.014.

[6] H. Zarringhalam, C. Majewski, N. Hopkinson, Degree of particle melt in Nylon-12 selective laser-sintered parts, Rapid Prototyping Journal. 15 (2009) 126–132. doi:http://dx.doi.org/10.1108/13552540910943423.

[7] U. Ajoku, Investigating the Compression Properties of Selective Laser Sintered Nylon-12, Loughborough University, 2008. https://dspace.lboro.ac.uk/2134/8095 (accessed December 15, 2016).

[8] C. Buckley, Structure of Polycrystalline Aggregates, in: E. Piorkowska, G.C. Rutledge (Eds.), Handbook of Polymer Crystallization, Wiley, Somerset, UNITED STATES, 2013. http://ebookcentral.proquest.com/lib/utxa/detail.action?docID=1209630 (accessed February 20, 2018).

[9] S. Kalpakjian, S.R. Schmid, Manufacturing engineering and technology, Seventh edition, Pearson, Upper Saddle River, NJ, 2014.

[10] B. Caulfield, P.E. McHugh, S. Lohfeld, Dependence of mechanical properties of polyamide components on build parameters in the SLS process, JOURNAL OF MATERIALS PROCESSING TECHNOLOGY. 182 (2007) 477–488. doi:10.1016/j.matprotec.2006.09.007.

[11] H.C.H. Ho, I. Gibson, W.L. Cheung, Effects of energy density on morphology and properties of selective laser sintered polycarbonate, Journal of Materials Processing Technology. 89–90 (1999) 204–210. doi:10.1016/S0924-0136(99)00007-2.

[12] Optical Coherence Tomography With NIR/SWIR | Sensors Unlimited, (n.d.). http://www.sensorsinc.com/applications/medical/optical-coherence-tomography (accessed September 12, 2016).

[13] W. Drexler, J.G. Fujimoto, Optical coherence tomography: technology and applications, Second edition., SpringerReference, Cham, 2015. http://ezproxy.lib.utexas.edu/login?url=http://link.springer.com/10.1007/978-3-319-06419-2 (accessed June 28, 2016).

[14] W. Wroe, J. Gladstone, T. Phillips, A. McElroy, S. Fish, J. Beaman, In-Situ Thermal Image Correlation with Mechanical Properties of Nylon-12 in SLS, in: Materials, Austin, TX, 2015.
[15] S. Fish, S. Kubiak, W. Wroe, J. Booth, A. Bryant, J. Beaman, A High Temperature Polymer Selective Laser Sintering Testbed for Controls Research, in: Process Development, Austin, TX, 2015.
[16] R.D. Goodridge, C.J. Tuck, R.J.M. Hague, Laser sintering of polyamides and other polymers, Progress in Materials Science. 57 (2012) 229–267. doi:10.1016/j.pmatsci.2011.04.001.
[17] D.L. Bourell, M.C. Leu, D.W. Rosen, Roadmap for Additive Manufacturing: Identifying the Future of Freeform Processing, 2009. https://wohlersassociates.com/roadmap2009A.pdf.
[18] J. Pellegrino, T. Makila, S. McQueen, E. Taylor, Measurement Science Roadmap for Polymer-Based Additive Manfucturing, Energetics Incorporated, 2016. https://doi.org/10.6028/NIST.AMS.100-5.
[19] A. Neef, V. Seyda, D. Herzog, C. Emmelmann, Low Coherence Interferometry in Selective Laser Melting, Physics Procedia. 56 (2014) 82–89. doi:10.1016/j.phpro.2014.08.100.
[20] J.A. Kanko, A.P. Sibley, J.M. Fraser, In situ morphology-based defect detection of selective laser melting through inline coherent imaging, Journal of Materials Processing Tech. 231 (2016) 488–500. doi:10.1016/j.jmatprotec.2015.12.024.
[21] G. Guan, M. Hirsch, Z.H. Lu, D.T.D. Childs, S.J. Matcher, R. Goodridge, K.M. Groom, A.T. Clare, Evaluation of selective laser sintering processes by optical coherence tomography, Materials & Design. 88 (2015) 837–846. doi:10.1016/j.matdes.2015.09.084.
[22] G. Guan, M. Hirsch, W.P. Syam, R.K. Leach, Z. Huang, A.T. Clare, Loose powder detection and surface characterization in selective laser sintering via optical coherence tomography, Proc. R. Soc. A. 472 (2016) 20160201. doi:10.1098/rspa.2016.0201.
[23] A. Lewis, M. Gardner, A. McElroy, T. Milner, S. Fish, J. Beaman, In-Situ Process Monitoring and Ex-Situ Part Quality Assessment of Selective Laser Sintering Using Optical Coherence Tomography, in: Process Development, Austin, TX, 2016.
[24] J. Veilleux, C. Moreau, D. Lévesque, M.L. Dufour, M. Boulos, Particle size measurement in glass powder beds using optical coherence tomography, OE, OPEGAR. 47 (2008) 033601. doi:10.1117/1.2896455.
[25] Nylon 12, (n.d.). http://polymerdatabase.com/polymers/nylon12.html (accessed July 6, 2016).
[26] A.D. Lewis, N. Katta, A.B. McElroy, T.E. Milner, S. Fish, J.J. Beaman, Understanding and improving optical coherence tomography imaging depth in selective laser sintering nylon 12 parts and powder, OE, OPEGAR. 57 (2018) 041414. doi:10.1117/1.OE.57.4.041414.

[27] A. Lewis, N. Katta, A. McElroy, T. Milner, S. Fish, J. Beaman, Investigation of Optical Coherence Tomography Imaging in Nylon 12 Powder, in: Process Development, Austin, TX, 2017.
[28] Ethyl cinnamate 112372, Sigma-Aldrich. (n.d.). http://www.sigmaaldrich.com/catalog/product/aldrich/112372 (accessed June 22, 2017).
[29] J. Schindelin, I. Arganda-carreras, E. Frise, V. Kaynig, Fiji: an open-source platform for biological-image analysis, Nature Methods. 9 (2012) 676. doi:10.1038/nmeth.2019.
[30] C.A. Schneider, W.S. Rasband, K.W. Eliceiri, NIH Image to ImageJ: 25 years of image analysis, Nature Methods. 9 (2012) 671. doi:10.1038/nmeth.2089.
[31] M.E. Brezinski, Optical coherence tomography: principles and applications, Academic Press, Amsterdam ; Boston, 2006.
[32] J. Rogowska, M.E. Brezinski, Evaluation of the adaptive speckle suppression filter for coronary optical coherence tomography imaging, IEEE Transactions on Medical Imaging. 19 (2000) 1261–1266. doi:10.1109/42.897820.
[33] K.M. Yung, S.L. Lee, J.M. Schmitt, Phase-Domain Processing of Optical Coherence Tomography Images, Journal of Biomedical Optics. 4 (1999) 125. doi:10.1117/1.429942.
[34] P.F. Stetson, F.G. Sommer, A. Macovski, Lesion contrast enhancement in medical ultrasound imaging, IEEE Transactions on Medical Imaging. 16 (1997) 416–425. doi:10.1109/42.611351.
[35] M.R. Gardner, A. Lewis, J. Park, A.B. McElroy, A.D. Estrada, S. Fish, J.J. Beaman, T.E. Milner, In situ process monitoring in selective laser sintering using optical coherence tomography, Optical Engineering. 57 (2018) 1. doi:10.1117/1.OE.57.4.041407.
[36] A. Buades, B. Coll, J.-M. Morel, Self-similarity-based image denoising, Communications of the ACM. 54 (2011) 109–117.
[37] J. Darbon, A. Cunha, T.. Chan, S. Osher, G.. Jensen, Fast nonlocal filtering applied to electron cryomicroscopy, in: 2008 5th IEEE International Symposium on Biomedical Imaging: From Nano to Macro, IEEE, 2008: pp. 1331–1334. doi:10.1109/ISBI.2008.4541250.
[38] T. Wagner, P. Behnel, ij-nl-means: Non local means 1.4.6 DOI: 10.5281/zenodo.47468, 2016. http://zenodo.org/record/47468 (accessed July 13, 2016).
[39] K. Dabov, A. Foi, V. Katkovnik, K. Egiazarian, Image denoising with block-matching and 3D filtering, in: Image Processing: Algorithms and Systems, Neural Networks, and Machine Learning, International Society for Optics and Photonics, 2006: p. 606414. doi:10.1117/12.643267.
[40] A. Lewis, S. Fish, J. Beaman, Capabilities and Limitations of Optical Coherence Tomography as an In-Situ Sensor for Curl and Porosity Detection in Selective Laser Sintering of Nylon 12, in: New Developments in Measurement Techniques, Sheffield, United Kingdom, 2019.

[41] A. Wegner, G. Witt, Correlation of Process Parameters and Part Properties in Laser Sintering using Response Surface Modeling, Physics Procedia. 39 (2012) 480–490. doi:10.1016/j.phpro.2012.10.064.
[42] S. Clijsters, T. Craeghs, S. Buls, K. Kempen, In situ quality control of the selective laser melting process using a high-speed, real-time melt pool monitoring system, The International Journal of Advanced Manufacturing Technology. 75 (2014) 1089–1101. doi:10.1007/s00170-014-6214-8.
[43] E. Bousi, I. Zouvani, C. Pitris, Lateral resolution improvement of oversampled OCT images using Capon estimation of weighted subvolume contribution, BIOMEDICAL OPTICS EXPRESS. 8 (2017) 1319–1331. doi:10.1364/BOE.8.001319.